STUDY ON LOCALIZED THERMAL EXPANSION GRADIENT FORMATION FOR ACOUSTIC WAVE GENERATION IN A NOVEL THERMOACOUSTIC IMAGING MODALITY

by

RUPAK BARDHAN ROY

Submitted to the Institute of Engineering and Natural Science
in partial fulfillment of
the requirements for the degree of
Doctor of Philosophy

Sabanci University

September 2017

Study on Localized Transient Thermal Expansion Gradient Formation for Acoustic Wave Generation in Novel Thermoacoustic Imaging Modality

APPROVED BY:

Assoc. Prof. Dr. Ayhan Bozkurt
(Thesis Supervisor) .....

Prof. Dr İbrahim Tekin .....

Prof. Dr. Serhat Yeşilyurt .....

Assoc. Prof. Dr. Arif Sanlı Ergün .....

Assoc. Prof. Dr. G. Göksenin Yaralıoğlu .....

DATE OF APPROVAL: 25/08/2017

ABSTRACT

STUDY ON LOCALIZED THERMAL EXPANSION GRADIENT FORMATION FOR ACOUSTIC WAVE GENERATION IN A NOVEL THERMOACOUSTIC IMAGING MODALITY

Rupak Bardhan Roy
Ph. D. in Electronics Engineering
Supervisor: Assc. Prof. Ayhan Bozkurt
September 2017

Thermoacoustics is the process of generation of sound by heat or vice versa. Volume generated thermoacoustic signals can be produced by thermal expansion induced volume contraction and rarefaction inside a target body. Thermoacoustic imaging uses this modality to obtain vivid insight into the internal structure of target body, both for non-destructive testing and biomedical imaging. Any penetrating pulsed radiation can be used for such purpose, including microwave where the modality is called thermoacoustics in general or by incident light waves where the same is termed as photoacoustics. The current thesis establishes the theoretical basis for a novel thermoacoustic imaging modality where pulsed ultrasound is used as the incident penetraing source. A formal forward transient theoretical eqution set is derived based on established transient acoustic propagation models and the problem is solved using a commercially available FEM software. The results are then compared with experimental results and considerable agreement has been observed.

Keywords : Thermoacoustics, AA-TAI, Analytical modeling, FEM.

ÖZET

YENİ BİR TERMOAKUSTİK GÖRÜNTÜLEME MODALİTESİNDE SES DALGASI ÜRETİMİ İÇİN LOKALİZE ISIL GENİŞLEME GRADYANI OLUŞTURULMASI ÜZERİNE ÇALIŞMA

Rupak Bardah Roy
Elektronik Mühendisliği Doktora Derecesi
Tez Yöneticisi: Doç. Dr. Ayhan Bozkurt
Ağustos 2017

Isı ile ses dalgası ve ses dalgalarıyla ısı üretilmesi, termoakustik adıyla anılmaktadır. Dış etmenlerle bir hacim içinde yaratılan sıcaklık değişimleri, sıkışma ya da genleşmeye neden olarak termoakustik işareti üretmektedir. Termoakustik görüntüleme tekniği, bu modalitenin hasarsız muayene ve biyolojik dokuların incelemenesi için kullanımına dayanmaktadır. Isının bir mikrodalga kaynağı tarafından üretildiği durumda teknik radyoa-kustik görüntüleme olarak anılmakta olup, kaynagın bir lazer olması durumunda foto-akustik adını almaktadır. Bu tezde, termoakustik işaretin üretilmesi için kullanılan ısı kaynağının ultrason dalgaları olduğu yeni bir görüntüleme tekniğnin kuramsal altyapısı oluşturulmuştur. İleri yönlü bir kuramsal denklem dizisi geliştirilerek, önerilen görüntüleme yönteminin geçici zamanlı çözümlemesisin bir ticari FEM yazılımıyla gerçekleştirilmesi sağlanmıştır. Çözümleme sonuçları, deneysel verilerle karşılaştırılarak doğrulanmıştır.

Anahtar Kelimeler: termoakustik, AA-TAI, çözümlemeli modelleme. FEM.

In loving memory of my father.
To the wives of Ph.D. grads.
With deepest regards for Mustafa hocam.

ACKNOWLEDGMENTS

Foremost, I would like to express my sincere-most gratitude to my thesis advisor Dr. Ayhan Bozkurt; not only for his continuous guidance on my study and research, but also for his never ending patience, motivation, and support in every aspect of my Ph.D. life. He has been the source of all my hard work and courage during the difficult and stressful times. I wish every Ph.D. student gets someone like him as an advisor. I could not have imagined having a better mentor ever.

Besides, I would like to thank my thesis committee: Prof. Ibrahim Tekin, Prof. Serhat Yesilyurt, and Assc. Prof. Arif Sanli Ergun and Assc. Prof. Goksenin Yaralioglu for their encouragement, insightful comments, and questions. My special gratitude and regards to Serhat sir for his advise during the toughest times. I owe my interest in COMSOL and analytical modeling to him. My heart-filled respect to Professor Mustafa Karaman of ITU.

I will be rightful to say that, half of this dream belongs to my mother. She has been the source of all the motivation behind my academic aspirations. If our society would have been a little supportive she would have been a successful mathematician. This is for your mom!

Whatever I say about you, my dear wife, it can never be enough. Only we know what we have been through all these years and what tantrums you have managed to withstand. The stressful year of qualifying exams, the frightening crises throughout all these years, the grasp of overwhelming loneliness and what not. I thrive only because you exist in my life!

Jethu, you are the reason I have made it this far. My deepest love and regards to you. My entire family, especially the bunch of my lovely cousins (Fazla!),rimi, didia, babai and sweetest mamoni back home, I love you guys. Be there always.

To all my friends, especially Kaustubh, Arka, Agnish, to some extent you have defined what I am today. Prabirda, Chitralidi and Manoneeta, I cannot forget your never-ending support, and the wonderful whole-nighters filled with joy and laughter. My special regards to Pandian bhai, Dilek, Parveen for all your support. Jaime, I cherish the long insightful conversation we had. I owe a lot to my labmates, especially Omid. You have been like a brother.

I have always been among those few fortunate people. A life with friends, family and dear ones full of support and encouragement. The list never ends. I feel it to be my duty to apologize to you all whose individual names are missing. You are a part of my life and I owe it all to you.

And finally, to all those people who have tried to make my journeys harder and stressful, I owe you a million thanks.

"......rebel soul shines like a diamond pulled from dust: bright, clear and flawless"
- Jay Long

Contents

List of Figures

List of Tables

List of Symbols

p_0 - Ambient pressure

p - Pressure perturbation

p_t - Total pressure

ρ_0 - Ambient density

ρ - Density perturbation

ρ_t - Total density

T_0 - Ambient temperature

T - Temperature perturbation

T_t - Total temperature

$\overrightarrow{v_0}$ - Ambient background velocity

$\overrightarrow{v}$ - Velocity perturbation

$\overrightarrow{v_t}$ - Total velocity

t - Time

∇ - Gradient operator

$\frac{\partial}{\partial t}$ - Partial time derivative

$\frac{\partial^2}{\partial t^2}$ - Partial second time derivative

M - Continuity equation source term

σ - Total stress tensor

δ_{ik} - Kroneckar delta in index notation

μ - Dynamic or shear viscosity

μ_B - Bulk viscosity

F - Momentum equation source term

$\frac{D}{Dt}$ - Material derivative

C_p - Heat capacity at constant pressure

α - Thermal expansion coefficient q - Heat flux

Φ - Viscous dissipation function

σ_{ik} - Viscous stress tensor

k - Thermal conductivity

Q - Energy equation source term

β - Isothermal compressibility

γ - Ratio of specific heat

c - Velocity of sound in medium

ϵ - Change in strain

T_{ref} - Reference temperature

$\overrightarrow{u}$ - Displacement

$\mathbf{F}_V$ - Volume force

ϵvol - Volumetric strain

ϵdev - Deviatoric strain

$\frac{d}{dt}$ - Time derivative

Q_m - Nonlinear acoustic source

p_s - Normal component of stress

β_1 - Coefficient of acoustic nonlinearity

A , B - Nonlinear acoustic parameters

$an1(t) = A(t)$ - Analytical function

p_S - Source pressure peak value

f_0 - Source signal frequency

$p(t)$ - Source pressure signal

T_{trunc} - Source signal truncation time value

h_0 - Maximum allowable mesh element size

N - Number of mesh elements per wavelength

CFL - Courant Friedrichs Lewy condition value

Δ_t - Time step

Chapter 1

Introduction

The word 'thermoacoustics' can be defined as 'the production of sound by heat' and vice versa. When heat is incorporated to a body, thermal expansion is made to do mechanical work [1], and it is the mechanical vibration of the body itself. The concept of thermoacoustics is centuries old, but, it is more recently that the acoustic and ultrasound research community has taken up the subject very seriously. The hard work has led to amazing discoveries in the field of vibration science and to cutting edge application. Some examples are cryocoolers, the Rijke tube, thermoelectric cooling, etc. In metals and other nonliving objects the technique offers a new method of non destructive evaluation (NDE). In such cases thermoacoustic effect can be used to differentiate and locate regions of varying mechanical, electrical, and thermal properties like thermal expansion coefficient, heat capacity etc. which conventional NDE fails to sense. The most recent event in the field is the invention of the thermoacoustic computed tomography or medical thermoacoustic imaging (TAI) which got introduced to the scientific community not more than three decades ago [2]. In such systems a pulsed energy source is used to excite a target region of the human body. The pulsed excitation induces some temperature expansion-rarefaction in the target region depending on the local physical, electrical or optical properties. This thermal expansion results in low amplitude acoustic wave that can be detected at finite distance.Acoustic waves generated by thermoacoustic principle with ionizing, radiating, electrical energy are generically termed as thermoacoustic effect. Photo-acoustic effect is the name given to the modality when incident radiation is light.

The elementary theory of thermoacoustics is based on the work by Lord Rayleigh [3] and Sondhauss [4], however most of the theoretical and experimental work were based only on the production of sound by heat. In 1850, Sondhauss experimentally investigated the oscillations related to glass blowers showing that sound frequency and intensity depends on the length and volume of the bulb followed by Kirchoff's publication on theoretical calculations on sound production by heat in 1868. Thermoacoustic effect with photon excitation was first reported by Alexander Graham Bell where he and Mr. Sumner Tainter investigated the sound production (audible range) by incident light [5]. The work focused on many metals but mainly on Selenium and claimed that various intensities of sound are produced from various materials when similar light intensity and frequency are incident. Hard rubber was seen to produce largest intensity whereas paper and mica produced the least. The first ever adaptation of the prevalent thermoacoustic effect in medical imaging was in 1980's by Professor Theoder Bowen of University of Arizona [2, 6]. Following these publications the scientific community dedicated itself to the investigation of thermoacoustic imaging principle for in-vivo and in-vitro experiments. Some old and recent literature deals with system design for microwave induced thermoacoustic imaging for breast cancer detection [7], thermoacoustic imaging of human arm using simple CRTs [8], development of fast parallel data acquisition systems for TAI [9], FEM system design for photoacoustic imaging procedure [10, 11], and a series of papers from the Indiana University Medical Center by Dr Robert A. Kruger. Kruger's publications started with a time averaged theoretical model of the photoaoustic effect where he assumed that a portion of photon energy is absorbed and being converted into heat [12]. Under such assumption he solved a modified version of Penne's Bioheat Transfer Equation (BHTE) with a heat source term. Then introducing the wave equation and under certain assumption incorporating the temporal temperature variation one can find the pressure at the detector. In the next paper of the series, some technical considerations were vividly discussed including the choice of irradiation frequency for RF based thermoacoustic imaging and a inverse Fourier transform based image reconstruction algorithm [13]. The paper also talked about an experimental setup for doing thermoacoustic computed tomography for imaging

the kidney. The detector set up was 64 elements of linear piezoelectric transducer arranged in a spiral manner. The RF excitation frequency was optimized as 434 MHz. The theoretical base of the considerations in the paper was taken from the assumptions used in the photoacoustic imaging model of the previous paper. Next two papers were published in 'Radiology Technical Developments'. First one published some imaging data with the previously developed experimental setup. The experiments were done in-vitro on porcine kidneys [14]. The results demonstrated comparative images between ultrasonography, MR and thermoacoustics, which formed the platform for in-vivo experiments on human breast in his next paper [15]. The results proved that thermoacoustic images can exhibit clear contrast-difference between healthy tissues and carcinoma. The final paper in the series set up a new experimental setup with linear transducer array where the sample was rotated with a rotor. So, the linear transducer array, even being fixed, was able to capture image of the entire sample [16]. Kruger's theoretical and technical considerations were accepted with high impact in the scientific community and were cited in numerous thermoacoustic research in the following years. One such publication introduced a better version of Kruger's system design, data acquisition and reconstruction algorithm which resulted in volumetric 3D thermoacoustic images [17]. In-vitro imaging was done on tumor mimics and breast models with acceptable results. In agreement with Kruger's comparative results of TA images and other conventional imaging modalities, the prior advantages can be categorized as:

- In soft tissue regions of the body the technique can provide important insight to tissue characteristics which conventional imaging modalities that predominantly depend on reflections fail to deliver.
- Thermoacoustic imaging has the capability to verify treatment procedures. For example, in cancer therapy using radiation or High Intensity Focused Ultrasound (HIFU), it can be used to understand the after effects of dosage delivery. Some recent research has successfully verified the claim by showing that HIFU Lesion shape and size can be studied both in-vitro and in-vivo during and after HIFU treatment [18].

In photoacoustic/thermoacoustic imaging, target tissue is illuminated with a short

laser/microwave pulse of very short duration (1 μs or less). Under thermal confinement conditions (i.e., heat generated at a point does not get enough time to diffuse), the temperature increase is directly proportional to the momentary absorption of energy. The resultant thermal expansion of the heated tissue creates an acoustic signal, which form the basis of thermoacoustic (TA) imaging. The analytical formulation of the theory has been deduced in available literature [19,20], and is based on the mathematical platform of reverse source problem. In both the cases (RF and Photoacoustics) the target is exposed homogeneously to the incident pulsed radiation. Thus, the dissipation of incident wave throughout the entire propagation path plays an important role. The nonlinear dissipation can be controlled if transmit beam-forming can be used; but none has been reported in available literature. Additionally, since both RF and LASER thermoacoustic uses electromagnetic incident radiation (though at different frequencies), the resultant TA wave in both cases exhibit closely related material properties.

Recently, a novel TAI imaging technique was proposed and named as 'Acousto-Acoustics' or 'All-Acoustic-TAI (AA-TAI)' by Prof. Mustafa Karaman of Istanbul Technical University (ITU). Experiments conducted by Prof. Karaman in association with Prof. Arif Sanli Ergun of TOBB-ETU, Ankara, provided evidence for the feasibility of AA-TAI. In the proposed technique, the thermoacoustic source itself is an ultrasonic pulse, so that the imaging sequence becomes all-acoustic, starting from pulsed energy incorporation, inducing thermal oscillations and up to the detection. Acoustic transmit beam-forming (focused ultrasound pulses) are used as the incident radiation and the modality is expected to provide realization of important acoustic properties of the target body which has not been reported by any available TA modalities in use. One important difference of the ultrasound-induced thermo-acoustic signal from its photo/microwave counterpart is the comparatively slow propagation velocity of incident sound compared to EM waves. Hence, the AA-TAI signals coming from the deeper tissue locations are delayed by the comparatively slow propagation speed of sound. In the contrary, photon and microwave induction generates TA signal simultaneously from every point wherever the penetration has taken place. The delayed generation of the AA-TAI signal can be beneficial in improving the depth resolution of the resulting image. In other words, photoacoustic

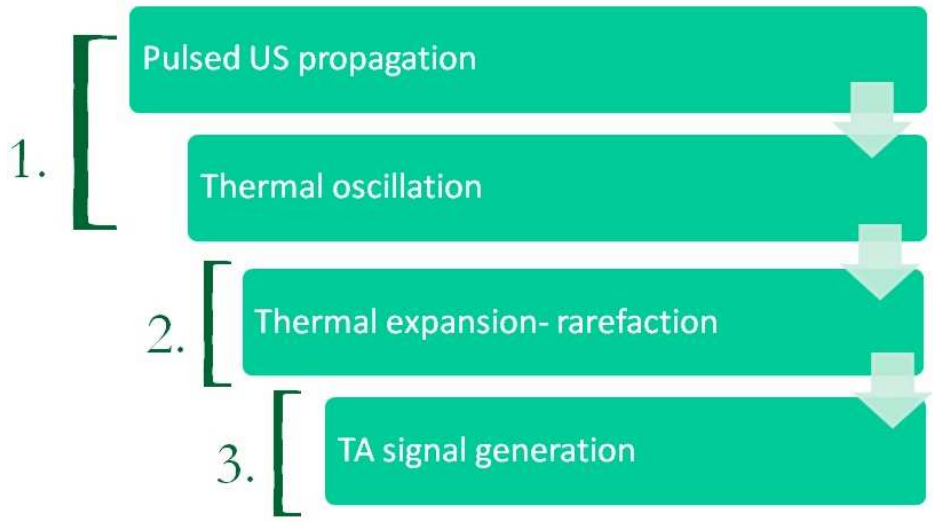

Figure 1.1: Flowchart for modeling process.

image resolution is limited by back projection of received array data (receive beam forming), where as, the AA image resolution utilizes both phased array transmit beam-forming as well as receive counterpart.

The aim of the current dissertation is the development of a forward transient theoretical model of the proposed modality to support the experimental findings of Prof. Mustafa Karaman, and Prof. Arif Sanli Ergun. The novelty of this current thesis is based on two primary motivations:

1. Forward transient theoretical modeling: Proposes a forward transient governing equation set and solves the same using commercially available FEM software. The schematic in Fig. 1.1 demonstrate the modeling steps. (1) The acoustic propagation of incident pulsed ultrasound and the thermal oscillation induced by the same are modeled using a set of equations. (2) Temperature output from the first set is used to solve for thermal expansion-rarefaction. (3) The final equation set uses the thermal expansion result to solve for the TA signal generation and propagation. Finally, some experimental results are used to prove the proposed model.

2. Manufacturing of high-efficiency transducers to be used in an imaging system based on AA-TAI.

Results obtained from simulations based on the developed model, which closely match experimental findings, are expected to shed light upon the virtues of the proposed thermoacoustic imaging modality. Numerical results are expected to be used in the assessment of signal levels to be received form various types of tissue, as well as the development of image reconstruction algorithms, and hardware components to support the proposed imaging technique.

The thesis has been organized as the following:

- Theory
- FEM simulation
- Model verification by experimental data
- CMUT for HIFU
- Conclusion

Chapter 2

Theory

The mechanism by which pulses of heat is generated inside a body (rather than only near the surface) by any form of pulsed penetrating energy is termed as volume heating. The heat rise and dissipation results in volume contraction and rarefaction which can form a acoustic source. The thermal stress produced in the body is very short lived. For the All-Acoustic-TAI (AA-TAI) modality in context, the analytical formulation has to be transient as the transit time of propagation of input and output acoustic pulses cannot be neglected. The focused sound can heat a small region of interest and by changing the direction of the transmit beam thermoacoustic signals can be generated and assembled by post processing. A somewhat longer time between transmit pulses are needed for ultrasonic heating in comparison to RF or photo-acoustics as the speed of propagation through the medium of interest is comparatively less. The disadvantage which negated the use of ultrasound during the early ages of TAI can now be used as an advantage, as the volume heating in pulsed LIFU/HIFU will be concised and the accompanying scattered radiation will not surpass the thermoacoustic wave. Alternatively, the technique of reverse polarization as discussed previously can be used.

A pulse of focused ultrasound (having a finite propagation time) incident in a volume of a solid evidently means a sudden fluctuation of stress around the steady state stabilized pressure value. The thermal oscillations due to the incident pulse can be modeled as simple energy transformation from the mechanical domain to heat domain and can be expressed by an approximated form of the energy equation

deduced from the first law of thermodynamics, which states;

$$Total\ Energy\ Change\ =\ Total\ input\ heat\ flux\ +\ Total\ work\ done\ on\ the\ body$$

The approximation is in considerable agreement with Tominaga [21] where he proposed the thermodynamic basis of thermoacoustics, stating:

> *"Heat flow, work flow and their mutual conversion all occur in a thermoacoustic device."*

Based on Tominaga's work, it can be stated in the mathematics to follow that the short lived thermal oscillations are directly linked to the fluctuation of the internal energy of the solid or the conversion of its mechanical energy to heat energy. This means that the periodic changes of stress originating from the acting LIFU/HIFU pulse on the body leads to periodic changes of temperature which finally lead to heat currents inside the body.

According to Clarence Zenner and J. B Alblas in their series of publications on the thermoelastic internal friction in solid [22–25], thermoelastic coupling is a physical phenomenon which is attributed to the coupling of the internal and mechanical co-ordinates of a solid body. Heat currents are generally associated with the increase of internal energy at the cost of mechanical energy. The conversion/increase of internal energy of a vibrating solid to/in-expense-of its mechanical energy is termed as internal friction. The coupling of the heat and mechanical coordinates of a solid is inherent with internal friction; and is termed as thermoelastic internal frictions in solid. This process of energy dissipation which is connected with the velocity of motion is the process of internal friction or viscosity. Both viscosity and thermal conductivity has considerable effect on transient acoustic heating of any media in question.

The viscous stress tensor (σ_{ik}) and its formulation for solids and liquids has been reported in numerous research published in the last few decades [26–31]. It is known that a perfectly elastic material can store 100% of its energy during deformation. On the contrary, there are materials which dissipate some of this energy, primarily in the form of heat. Since heat is dissipated, the stress strain curve during the loading and unloading phase of the motion is different from perfectly elastic case as shown in Fig. 2.1. The amount of heat dissipated or acoustic energy absorbed by the material

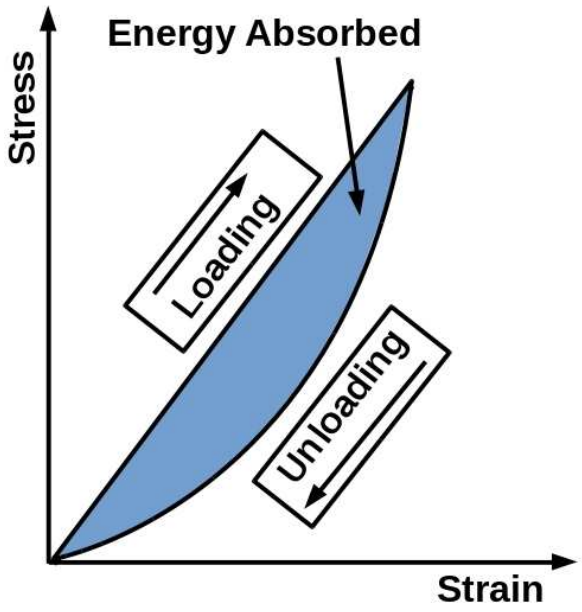

Figure 2.1: A schematic representation of hysteresis.

is the area between the loading and unloading curve; also known as hysteresis. Hysteresis requires that the loading portion of the stress-strain curve must be higher than the unloading curve. Thus, from a stress-strain curve we can see the hysteresis as the area between the loading and unloading curve. Real media are characterized by such stress relaxation, structural viscosity, etc. Unlike perfectly elastic material following Hooke's law, stress in such materials are thus dependent on both strain and its time derivative. Such materials are mainly biological media, polymers and sometime approximated for metals as well; only with very high viscosity values. The existing theory of viscosity or internal friction is globally used to describe the mechanical properties of such materials.

2.1 Equation set for transient heating by pulsed ultrasound

The transient heating by pulsed ultrasound propagation can thus be modeled using the conservation equations following the heat-work law of thermodynamics. For the current case where only pulses of ultrasound is the incident acoustic source, the

temporal variation of vibration as well as its effect on the variation of background temperature at the region of interest needs to be analyzed.The analytical modeling of transient acoustic heating in fluids and solids under the light of thermoviscous flow and thermoelasticity has been based on the approximation of traditional equation of conservation [24, 25, 32–35]. The current case, where both thermal conductivity and viscosity controls the phenomenon of thermal oscillation, is not an exception as well.

Let us consider a material with background mean flow density, pressure, velocity and temperature defined as ρ_0, p_0, $\overrightarrow{v_0}$, and T_0, respectively. For small change on these variables defined by ρ, p, $\overrightarrow{v}$ and T, the total variable quantities are defined as:

$$\rho_t = \rho + \rho_0 \tag{2.1}$$

$$p_t = p + p_0 \tag{2.2}$$

$$\overrightarrow{v_t} = \overrightarrow{v} + \overrightarrow{v_0} \tag{2.3}$$

$$T_t = T + T_0 \tag{2.4}$$

For the current case ρ_0 is the static density of the material in context, $p_0 = 0$, $\overrightarrow{v_0} = 0$ and $T_0 = 293.15$K. Thus the total pressure and velocity are equal to the change or perturbation and can be written as, $p_t = p$ and $\overrightarrow{v_t} = \overrightarrow{v}$ respectively. The propagation of sound pulse and the corresponding thermal oscillation can be modeled with the equations of mass, momentum and energy conservation [36] approximated for the given model in context and are given by:

$$\frac{\partial \rho_t}{\partial t} + \nabla \cdot (\rho_0 \overrightarrow{v}) = M \tag{2.5}$$

$$\rho_0 \frac{D\overrightarrow{v}}{Dt} = \nabla \cdot \sigma + F \tag{2.6}$$

$$\rho_0 C_p \left(\frac{\partial T_t}{\partial t} + (\overrightarrow{v} \cdot \nabla) T_0 \right) - \alpha T_0 \left(\frac{\partial p}{\partial t} \right) = -\nabla \cdot q + \Phi + Q \tag{2.7}$$

Eq. 2.5, Eq. 2.6 and Eq. 2.7 are also respectively termed as the Continuity, Navier-Stokes and Energy equations, where C_p is heat capacity at constant pressure, α is the coefficient of thermal expansion and M, F, Q are the respective source terms. The source terms are zero in the incident transmit case. The operator $\frac{D}{Dt}$ is the material derivative (or advection operator) defined as:

$$\frac{D}{Dt} = \frac{\partial}{\partial t} + (\overrightarrow{v} \cdot \overrightarrow{\nabla}) \tag{2.8}$$

Total stress tensor can be written in Stoke notation as:

$$\sigma = -p\delta_{ik} + \mu\left(\nabla\overrightarrow{v} + (\nabla\overrightarrow{v})^T\right) + \left(\mu_B - \frac{2}{3}\mu\right)(\nabla.\overrightarrow{v})\delta_{ik} \tag{2.9}$$

where μ and μ_B are the dynamic (shear) and bulk viscosity respectively. Finally, the viscous dissipation function and the heat flux(Fourier) is defined as:

$$\Phi = (\nabla\overrightarrow{v}).\sigma_{ik} \tag{2.10}$$

and

$$\mathbf{q} = -k(\nabla T) \tag{2.11}$$

k being the thermal conductivity and σ_{ik} being the viscous stress tensor given by

$$\sigma_{ik} = \mu\left(\nabla\overrightarrow{v} + (\nabla\overrightarrow{v})^T\right) + \left(\mu_B - \frac{2}{3}\mu\right)(\nabla.\overrightarrow{v})\delta_{ik} \tag{2.12}$$

where μ and μ_B are the shear and bulk viscosity of the medium in question. In index notation δ_{ik} is the Kronecker Delta function which is 1 when $i = k$, otherwise being 0. The equation set Eq. 2.5 to Eq. 2.7 is closed by the thermodynamic state equation given as:

$$\rho_t = \rho_0(\beta p - \alpha T_t) \tag{2.13}$$

where β is the isothermal compressibility given by $\beta = \frac{1}{\rho_0}\frac{\gamma}{c^2}$; c being the speed of sound in the medium and γ being the heat capacity ratio approximated to 1 for any material other than air.

2.2 Equation set for transient thermal expansion and volume displacement:

Thermal expansion can be modeled using the established thermal expansion equation given as:

$$\epsilon = \alpha(T_t - T_{ref}) \tag{2.14}$$

where ϵ is the change in strain; α,the thermal expansion coefficientT_{ref} is the reference temperature and the difference $(T_t - (T_{ref}))$ is the temperature variation, T_t being the total temperature obtained by solving the coupled conservation equations

in the previous module. The total displacement vector originating from the strain change can be resolved by solving the displacement equation given as:

$$\rho_0 \frac{\partial^2 \overrightarrow{u}}{\partial t^2} = \mathbf{F}_V - \nabla.\sigma \tag{2.15}$$

ρ_0 is the material density, $\mathbf{F}_V$ is the volume force and σ is the total stress which also includes the viscous stress component given by

$$\sigma_{ik} = \mu_B \frac{d\epsilon_{vol}}{dt} + \mu \frac{d\epsilon_{dev}}{dt} \tag{2.16}$$

ϵ_{vol} and ϵ_{dev} are the volume strain and deviatoric strain respectively. The strain Equation 2.14 can be expressed in the respective volume and deviatoric components. μ and μ_B are the shear and bulk viscosity components.

2.3 Equation set for AA-TA signal generation and propagation:

The TA signal generation and propagation problem is analyzed by solving the non-linear wave equation.

$$\frac{1}{\rho_0 c^2} \frac{\partial^2 p}{\partial t^2} - \nabla.(\frac{1}{\rho_0} \nabla p) = Q_m \tag{2.17}$$

where, the source term;

$$Q_m = \frac{\beta_1}{{\rho_0}^2 c^4} \frac{\partial^2 (p_s)^2}{\partial t^2} \tag{2.18}$$

p_s being the source pressure, which in this particular case is the normal stress originating from the thermal expansion. The solution of the wave equation yields the required thermoacoustic pressure signal. β_1 is the coefficient of acoustic non-linearity given by

$$\beta_1 = 1 + \frac{B}{2A} \tag{2.19}$$

where A and B are the nonlinear acoustic parameters. For water $\beta_1 = 10$.

In Eq. 2.5, Eq. 2.6, Eq. 2.7 the linear assumption promotes that temperature linearly follows the focal pressure. In the following set, thermal expansion is also modeled for a linear elastic model, however with viscous damping under consideration. Now, since the TA source term (Eq. 2.18) depends on the double derivative of the square of normal stress (derived from stresses developed during thermal

expansion-rarefaction) the volume generated TA signal must follow the envelope of the thermal expansion induced normal stress. Thus the output change must scale as the square of any input change. The Fourier analysis must have a strong DC component and a band around the frequency component of the envelope. Additionally surface generated TA signals can also be modeled as discussed by Bowen [2,6] in his pioneer papers. A small analysis at the beginning of Chapter 3 will discuss briefly where they differ from the volume generated TA signals, which is of prior concern for understanding the internal acoustic properties of a target body.

Chapter 3

FEM Simulation

The set of equations used to model transient acoustic heating by ultrasound pulses in Chapter 2 does not have an exact solution. Finite Element Analysis(FEA) simulations using COMSOL Multiphysics®, a commercially available FEM package by COMSOL Inc., Burlington MA is used to solve the entire set of equations starting from pressure propagation, thermal oscillation, TA signal generation and TA signal propagation. The conservation equation set is solved using the transient linear Navier–Stokes module. Thermal expansion is solved using the Solid Mechanics module. Pressure Acoustics module with nonlinear source term is used to solve for the TA signal generation and propagation. To understand the theory on a basic level a simple model is considered at first. Later the pulsed HIFU model is developed. Before the simulation results are demonstrated it is important to discuss the modeling process for both simple and HIFU model, which includes, geometry, material parameters, boundary conditions etc.

3.1 Geometry

3.1.1 Simple model geometry

The simple model is shown in Fig. 3.1. In the geometry, the smaller half circle represents the solid where as the bigger ring geometries represent liquid domain. The solid domain forms the TA source. An acoustic point source is defined near the geometry origin. Since in the linearized Navier–Stokes module a defined point

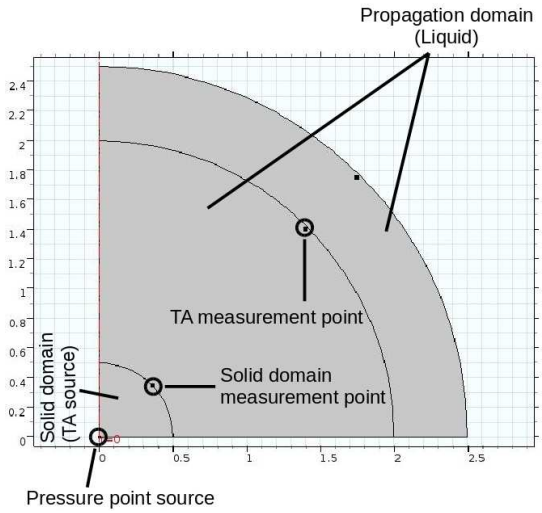

Figure 3.1: Model geometry

source is not available, it is defined as a tiny straight line (0.001 nm) on the horizontal axis. Since the model is axisymmetric the horizontal axis is attributed by the symmetry boundary condition, which indicates mirroring. In case of Navier–Stokes and nonlinear pressure acoustic modules the vertical axis (r=0) and the outer ring boundary are attributed with material impedance boundary condition. In the pressure acoustics module the solid domain (smaller inside quarter circle) is defined as the TA domain source.

3.1.2 HIFU model geometry

The HIFU model geometry is constructed step by step as shown in Fig. 3.2. The HIFU transducer half surface (as defined in general axisymmetric cases) is created by area intersection of a circle and a triangle. The circle Fig. 3.2(a) defines the curvature of the transducer and the focal point (25.4 mm, the center of curvature). A rectangle Fig. 3.2(b)is then drawn with the dimension of 6.35 mm by 0.8066 mm with one point at the origin. The intersection of the two structures forms the surface of the designated transmit transducer as shown in Fig. 3.2(c).The liquid loading domain is then added to the model as a 28.4 mm by 6.5 mm rectangle for transient analysis. The next step is to do the mathematical union of the two domains which automatically removes the intersection line by deselecting any internal boundary structures, hence making the structure continuous. as shown in Fig. 3.2(d). Finally

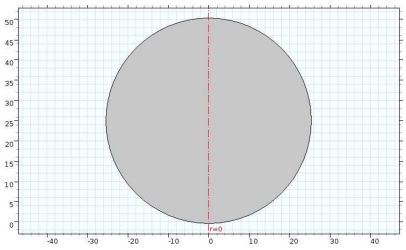

(a) 25.4 mm circle

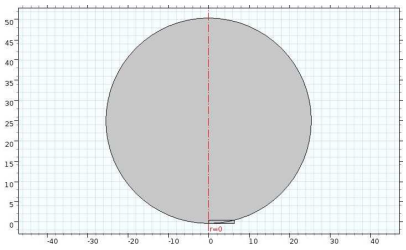

(b) 6.35 mm by 0.8066 mm rectangle

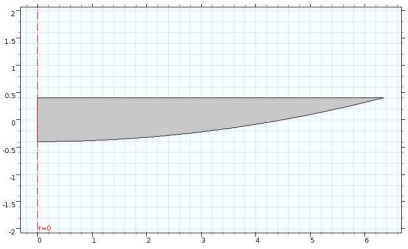

(c) Transducer half surface

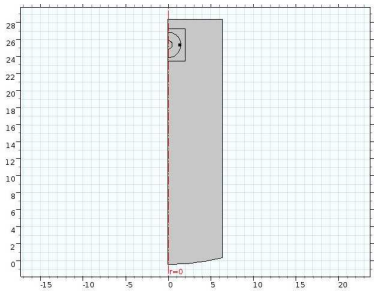

(d) Finalized geometry with immersed focal object.

Figure 3.2: Steps of defining the axisymmetric computation model geometry.

a semicircle of 0.5 mm radius is drawn around the focal point of the transducer which represent the immersed silicon glue stick bead as shown in Fig. 3.2(e). It is always useful to keep the analysis domain as small as possible for transient analysis to reduce the RAM usage. The RAM or physical memory needed for running a COMSOL transient simulation depends on the meshing. A denser mesh increases the memory usage. To negate the usage of large RAM and to reduce the computation time the results from an initial Navier–Stokes module solution is coupled to a smaller internal domain and the solution of thermal expansion, and TA signal generation is solved inside, as discussed later in the results. The small domain is defined by a 3.7 mm by 2 mm rectangle as shown in Fig. 3.2(e). The larger ring (only for structural meshing) around the glue bead is constructed by a 1.5 mm radius circle with the

center again at 25.4 mm. In the frequency domain characterization (for checking the focusing capability) of the HIFU transducer one needs to incorporate the absorbing boundary condition as the perfectly matching layer (PML). The geometry is similar with an additional 3 mm thick layer around the domain, defined as the PML. The internal boundaries of the PML was also removed with the union operation.

3.2 Modules

This is a short description of the multiphysics modules used for the HIFU model simulations. The model geometry as described above has a number of boundaries, domains and points of measurements. Fig. 3.3 has all of them marked and named accordingly.Domains DI, D2 and D3 represent the liquid water domain. The domain has been broken to facilitate the structured meshing scheme. D4 represents the solid material in question, which is a small silicon glue stick bead. Boundary B1 is the transducer surface where the time varying input pressure pulse is attributed. Point P1 is the focal point where pressure , temperature and thermal expansion induced displacement 1D plots are generated. The TA signal is gathered at point P2 In order

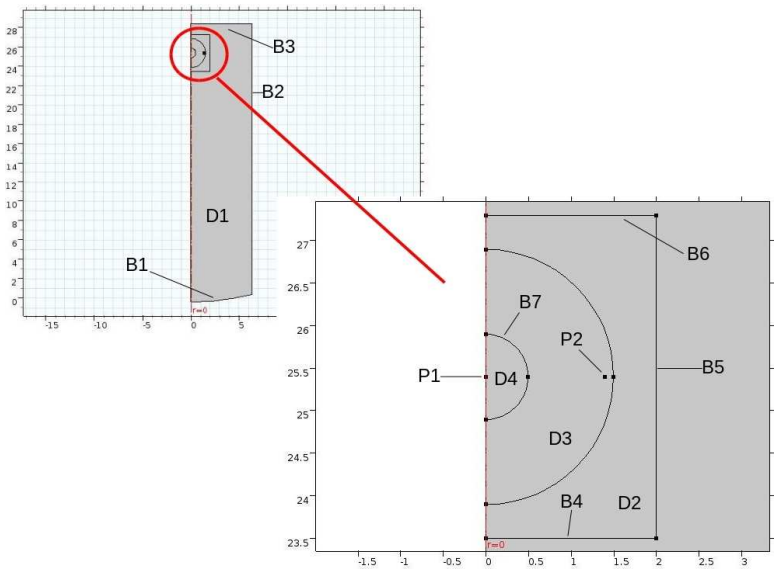

Figure 3.3: HIFU model: domain, boundary and points.

to understand the pulsed ultrasound HIFU pulse propagation and focusing, all the domains were selected under the transient Navier–Stokes module. B1 impersonates

the transducer surface and hence an analytical pressure function was incorporated to the surface but truncated at 400 ns to approximate the 5 MHz 2 cycle sinusoidal pulse. The analytical function is defined as,

$$an1(t) = A(t) = p_S Sin(2\pi f_0 t) \tag{3.1}$$

for t defined between 0 and 800 ns. The pressure on the transducer surface is defined as

$$p(t) = p_S * an1(t) * (t[s] < T_{trunc}) \tag{3.2}$$

$p_S = 100\ kPa$ is the peak input pressure, and can be manually defined as needed as an input parameter. For a f_0=5 MHz burst of 2 cycles, the period T is 400 ns. In order to make sure that the propagating waves do not reflect from the domain boundaries the characteristic acoustic impedance of water is set to boundaries B2 and B3; water being the liquid domain in context. To reduce the time and RAM requirements of the coupled simulations. The smaller geometry encircled by B4, B5 and B6 boundaries is used. The pressure coupled from the large Navier-Stokes simulation is couple to B4 by the 'withsol' function in COMSOL and defined as 'withsol('sol1',p,setval(t,t))' where 'p' is the pressure from the previous all domain Navier-Stokes computation, performed between 0 to 24 μs. For solving the coupled modules, the computation is done from 15 - 23 μs. B4 is attributed with the above noted 'withsol' function which is the input pressure boundary for the smaller domain. Characteristic acoustic impedance of water was again incorporated to the boundaries B5 and B6.

The temperature variation from the Navier-Stoke module is used to compute transient volume thermal expansion of the solid domain. The 'Thermal Expansion' sub-node comes under the Solid Mechanics module. Only the silicone glue domain D4 is selected under the same. Thermal expansion leads to internal contraction and rarefaction and displacement. The solid boundary B7 is configured to be 'free' for displacement. The pressure acoustic transient module is used to solve for the TA pressure signal. The source term is incorporated to the solid D4. Boundaries B4, B5 and B6 are incorporated with characteristic impedance of water. The 1D plot of TA signal is gathered for analysis at the point P2.

3.3 Materials

The liquid domain used is water with the material properties stated in Table. 3.1. Table. 3.2 below depicts the material properties of the silicone glue stick [30].

Table 3.1: Property parameter of Water

Parameter	Value
Velocity of sound	1480 m/s
Density	1000 Kg/m^3
Specific heat	4185.5 J/Kg-K
Thermal conductivity	0.598 W/m.K
Coefficient of thermal expansion	2×10^{-4}
Bulk viscosity	3.09×10^{-4} Pa-s
Dynamic viscosity	8.09×10^{-4} Pa-s

Table 3.2: Property parameter of Silicone glue stick

Parameter	Value
Velocity of sound	1345 m/s
Density	1100 Kg/m^3
Specific heat	1200 J/Kg-K
Thermal conductivity	1.9 W/m.K
Coefficient of thermal expansion	7×10^{-4}
Bulk viscosity	10 Pa-s
Dynamic viscosity	20 Pa-s
Young's modulus	0.025 GPa
Poisson's ratio	0.48
β_1	4

3.4 Meshing and time stepping

Any time dependent equations has a band of frequencies in the solution. To resolve these frequencies, the maximum allowed mesh element size becomes,

$$h_0 = \frac{c}{(N \cdot f_0)} \tag{3.3}$$

where c is the local speed of sound, and N is the number of mesh elements per wavelength in the minimal case. A finer mesh means a bigger N. Choosing a time step that resolves the wave equally well in time (as the mesh does in space) is

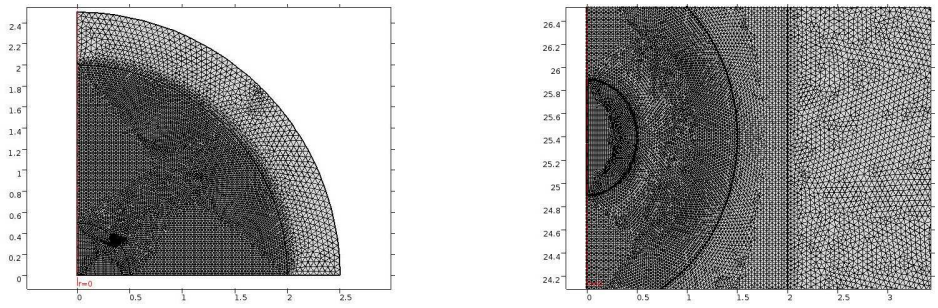

(a) Mesh structure for the simple model. (b) Mesh interaction in the HIFU medel.

Figure 3.4: Meshing.

also very important. Longer time step fails to make optimal use of the mesh, and smaller time step leads to longer solution times with not much improvement on the results. The relationship between mesh size and time step length is defined by the Courant Friedrichs Lewy(CFL) condition number:

$$CFL = \frac{c \cdot \Delta t}{h_0} \tag{3.4}$$

or;

$$\Delta t = \frac{(CFL) \cdot h_0}{c} \tag{3.5}$$

where Δt is the time step and h_0 is the maximum mesh element size. In practice, CFL number of 0.2 proves can be used as an optimal case.

For the HIFU model geometry the smaller circle is the solid which is meshed with N=12 ($h_0 = 22.416\,\mu$m) and the water domain is structurally meshed. The bigger ring area is a densely meshed with N=10 ($h_0 = 29.6\,\mu$m), the rectangular area with N=8 ($h_0 = 37\,\mu$m) and the bigger water domain with N=5 ($h_0 = 59.2\,\mu$m). These values are calculated assuming $f_0 = 5$MHz, $c = 1480\,$m/s for water and $c = 1345\,$m/s for silicone stick. The time step is optimized for $h_0 = 22.416\ \mu$m, $c = 1345\,$m/s and $CFL = 0.2$ yielding 3.3 ns. The mesh interaction between the solid and fluid interface for both the simple and HIFU model are shown in Fig. 3.4. Free rectangular elements have been used for meshing.

3.5 Results

In this section the simulation results for both the simple and HIFU model are analyzed in detail.

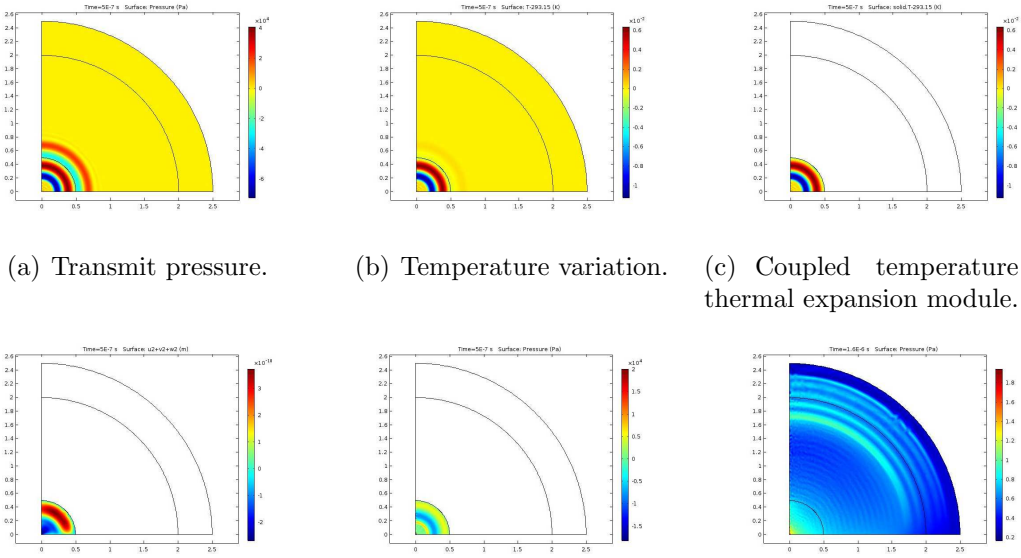

(a) Transmit pressure. (b) Temperature variation. (c) Coupled temperature to thermal expansion module.

(d) Solid displacement. (e) Normal stress on solid. (f) TA signal.

Figure 3.5: Qualitative analysis of volume TA signal generation for simple model with a 2 MPa, 2 cycle 5 MHz input.

3.5.1 Simple model

Some surface plots are generated for qualitative analysis. For instance, the incident pressure field, temperature, coupled temperature to solid domain and displacement surface plots for 2 MPa input are generated at 500 ns and exhibited in Fig. 3.5. The 1D plots of the coupled momentum and energy equation are visualized at the point near the solid boundary. For instance, for a 2 MPa input pulse; the pressure, its frequency component and linear temperature variation is shown in the Fig. 3.6. The input is a 2 cycle, 2 MPa, 5 MHz point pressure source. The temperature variation in the solid originating from Navier-Stokes and energy equation is coupled to the solid mechanics domain and thermal expansion induced displacement of the solid domain is solved with viscous damping in consideration. The viscosity can be found in Table 3.2. The displacement of the solid in the point of measurement (as same as for the input pressure and temperature) is shown in Fig. 3.6(d). For the defined input the pressure near the solid surface has a peak value of 20 kPa yielding an approximate peak temperature change of 4 mK. The peak displace is approximately 0.28 nm in context.

The domain pressure source is defined by the double time derivative of the squared pressure (or the normal component of stress originating from the thermal

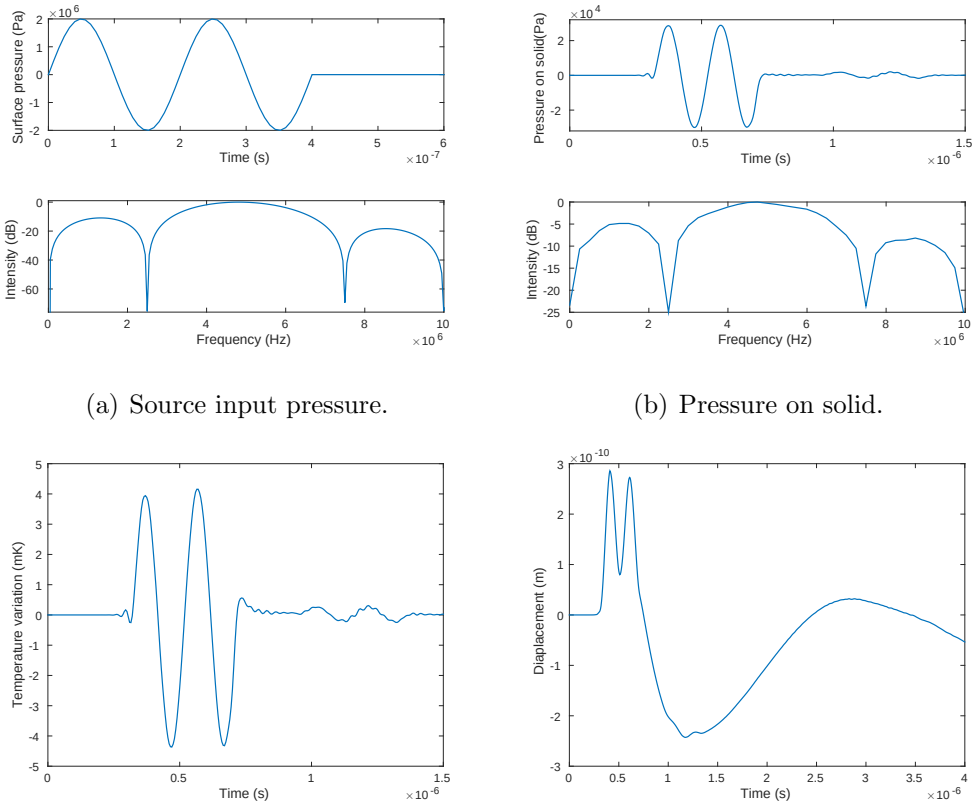

(a) Source input pressure.

(b) Pressure on solid.

(c) Temperature variation on solid.

(d) Thermal expansion induced displacement.

Figure 3.6: Pressure, temperature and displacement analysis in simple model.

contraction and rarefaction) scaled by the density square. The solution of the wave equation taking the normal stress as the nonlinear domain source yields the total TA signal pressure at the output and is measured at the boundary of the liquid domain. The TA signal must scale with the envelope of the normal stress component originating from thermal expansion. However, since the measurement in this case is done along the direction of the incident input wave, the envelop also contains higher frequency scattered signal components. This can be clearly seen in the Fig 3.7(a) where the Fourier analysis yields the frequency components. Since a 2 cycle sinusoid has been used, the TA envelop has a pass band around 1 MHz with a strong DC component, which can be clearly seen in the image. As a proof of the square dependence of the output TA signal on input sweep, a range of simulations were performed by changing the input peak from 1 Mpa to 8 MPa and the the highest peak pressure of the TA signal was plotted against each consecutive input. The data was compared with the quadratic curve in MATLAB and a perfect match was

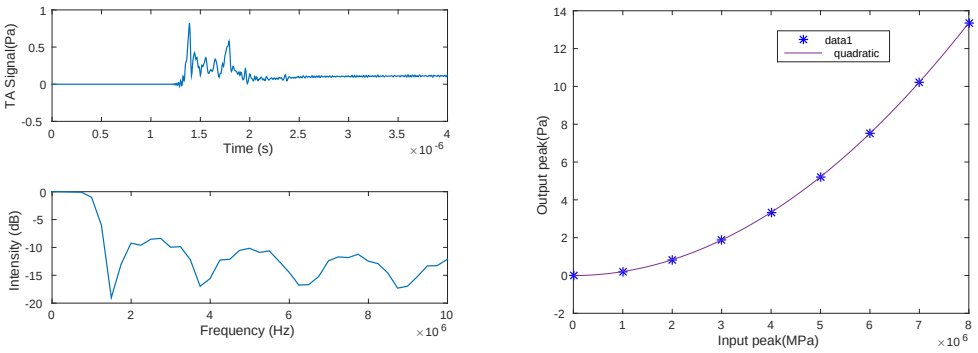

(a) TA signal and its frequency components. (b) Perfect square dependence of output on input.

Figure 3.7: Evaluation of the output TA and its square dependence on the input change. Since the TA measurement is done along the direction of input signal there are higher frequency components. The TA signal can be segregated by filtering the output.

observed.

If one uses only the solid boundary displacement as the source and solves the wave equation the output is not the envelope but rather a time varying signal with both scattered and surface generated TA signal. The propagating signal contains both the scattered 5 MHz signal and the surface generated TA signal. The TA signal scales non-linearly but not as an exact square of the input sweep. One can extract the TA signal by polarity cancellation; i.e. simply by summing the output generated from positive and negative polarity input. This means, if one has the output signals originating from a +2 MPa and -2 MPa input pressure pulses, then summing the two output will segregate the surface generated TA signal as the scattered 5 MHz component is 180° out of phase from the input. Evidently subtracting the two opposite polarity output will increase the strength of the scattered signal. From the images in Fig. 3.8 the idea can be clearly realized. The resonance of the surface generated TA signal is at 1 MHz as can be seen in Fig. 3.8(d). By varying the input peak pressure from 1 MPa to 4 Mpa and plotting the absolute peak pressure of the polarity canceled surface generated TA signal one obtains a nonlinear relation between the two, which doesnot exactly follow square law as can be seen in Fig. 3.8(e). A comparative spectral response of 2 MPa and 3 MPa input is also exhibited in Fig. 3.8(f). As an increase from 2 to 3 MPa implies a 1.5 times change in the input, for a square law variation one will expect a 7 dB increase in the spectral component.

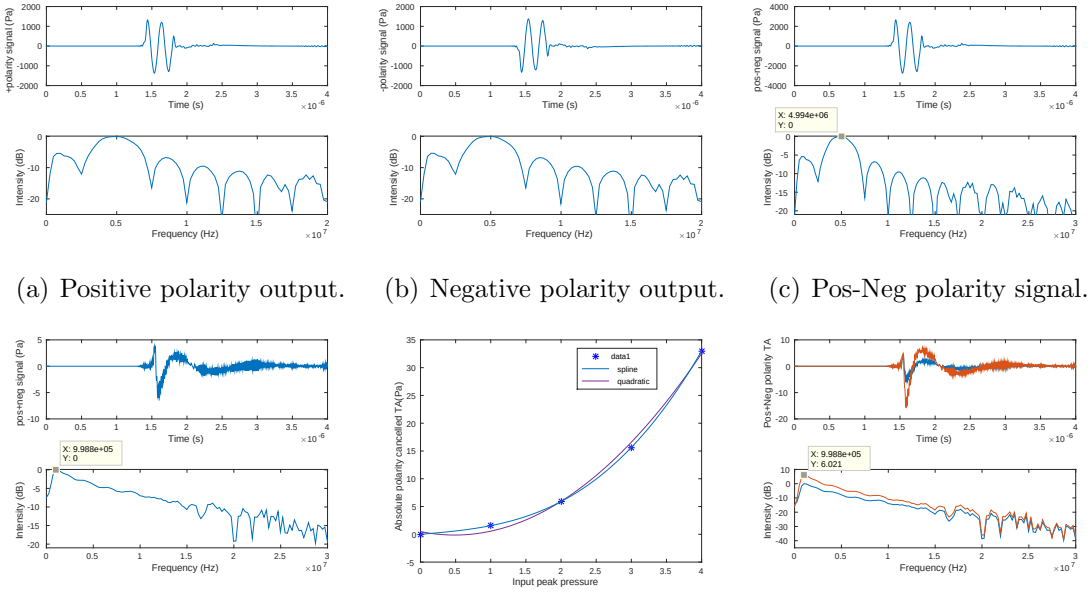

(a) Positive polarity output. (b) Negative polarity output. (c) Pos-Neg polarity signal.

(d) Pos+Neg polarity surface generated TA signal. (e) Nonlinear (not square) variation of TA signal absolute pressure. (f) Spectral comparison of TA for 2 MPa(blue) and 3MPa(red)input.

Figure 3.8: Evaluation of the output surface generated TA and scattered signal

In the contrary a 6.02 dB increase is observed.

3.5.2 Pulsed HIFU model

As we will discuss in Chapter 4, the transmit transducer is a single element fixed focus device with a center frequency of 5 MHz, radius of curvature (focal distance) of 25.4 mm and F number of 2. The surface of the transducer is modeled as the pressure source. A harmonic acoustic analysis is performed to characterize the focal capability of the transmit transducer. The 1D plot of normalized absolute pressure(Fig. 3.9(b))

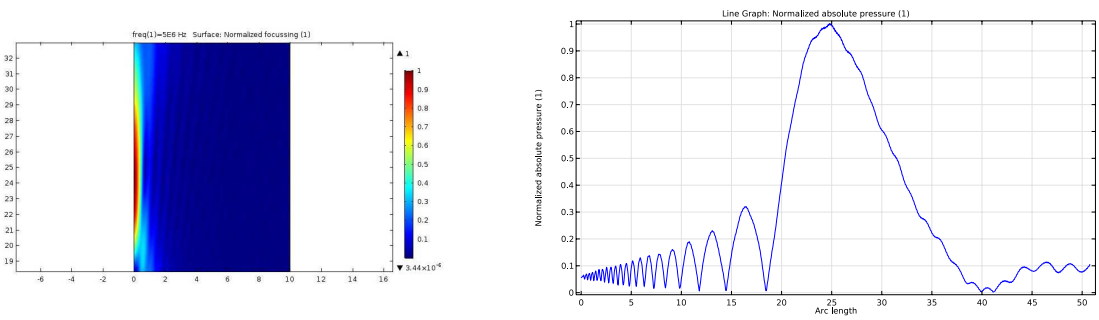

(a) A closeup look at the focal point. (b) 1D pressure plot.

Figure 3.9: Frequency domain characterization of the focal capability of the transducer.

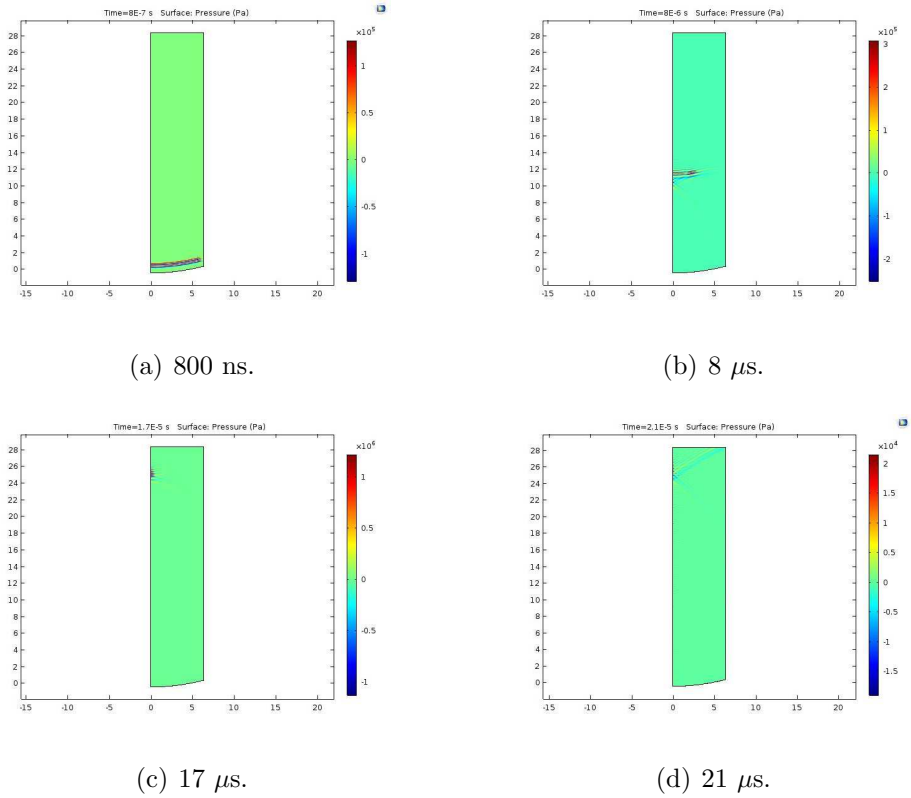

(a) 800 ns.

(b) 8 μs.

(c) 17 μs.

(d) 21 μs.

Figure 3.10: Temporal propagation of pressure field in water.Surface pressure is incorporated as 100 kPa.

along the axis of symmetry clearly indicates the focal spot around 25.4 mm, hence in congruence with the transmit transducer used in the experiments.

Transient pressure propagation

To characterize the transient HIFU pulse focusing, a propagation model in water domain(without solid) is solved at first. A 100 MPa 2 cycle 5 MHz pulse is applied to the transducer surface. Normal impedance boundary condition at the water domain boundary is incorporated to avoid reflection. Fig. 3.10(c) and Fig. 3.10(d) indicates transient focusing and boundary absorption. The small silicon glue stick bead is then inserted at the focal zone of the transducer. The acoustic focusing is computed for the entire domain within a time span of 0 to 24 μs. The time domain pressure data from the same is then incorporated to the smaller rectangular domain and the coupled TA problem is solved in the smaller domain only. Fig. 3.11 demonstrates the successful transfer of pressure propagation from entire model to the smaller region. The results in Fig. 3.12 shows the propagation of the focused pulse in the small

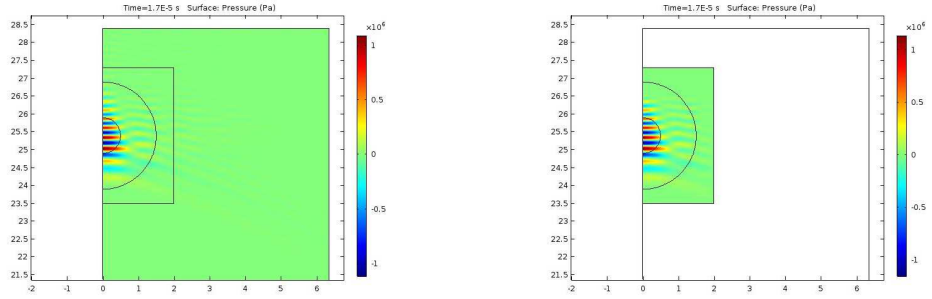

(a) Focal pressure computed in the large domain.

(b) Successful incorporation in the small domain

Figure 3.11: Coupled pressure data from large to small domain.

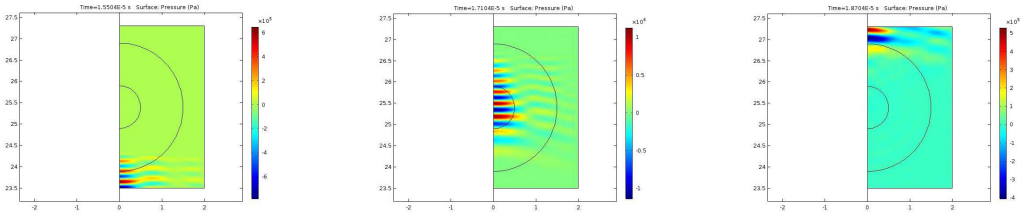

(a) 15.5 μs.

(b) 17.1 μs.

(c) 18.7 μs.

Figure 3.12: Transient pressure propagation through solid for 100 kPa 2 cycle 5MHz source.

domain. Acoustic wave absorption is clearly depicted in Fig. 3.12(c).

Transient thermal oscillation

The energy equation is solved with an initial domain temperature of 293.15° K. Fig. 3.13 exhibits some time shots of the thermal oscillations. The successive heating and cooling which follows the positive and negative cycle of the pressure pulse is a proof of acoustic heating and cooling effect evident in a thermoacoustic device. A thermoacoustic refrigerator pumps heat from low temperature to high temperature region using sound. The source of acoustic energy can be a loudspeaker which emits sound waves in a resonator filled with gas at high pressure. The frequency of the driver and the length of the resonator are chosen so as to get a standing pressure wave in the resonator. A porous material like a stack of plates is used in the acoustic path. Due to the thermal effect of sound one end heats up while the other cools down. A refrigeration load can then be applied at the cold end by means of a heat exchanger.

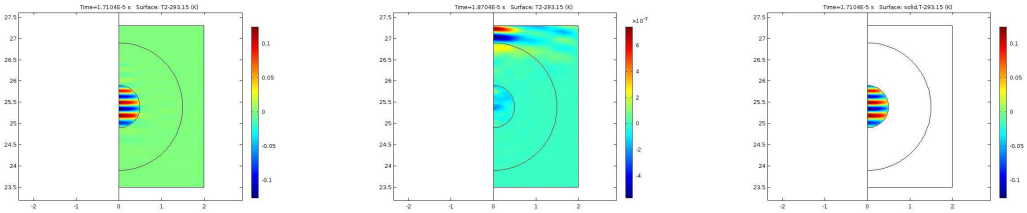

(a) 17.1 μs. (b) 18.7 μs. (c) Temperature coupling 17.1 μs.

Figure 3.13: Temperature variation at focus and (c) Coupled temperature to solid (thermal expansion) domain.

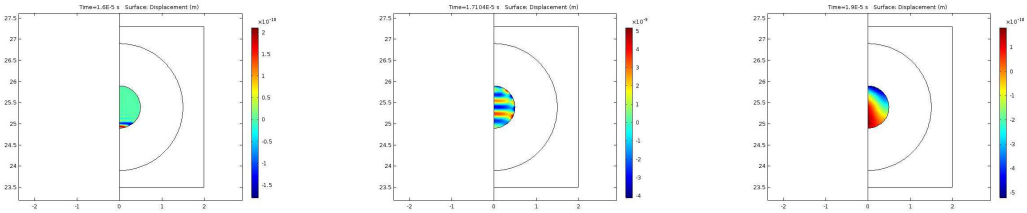

(a) 16 μs. (b) 17.1 μs. (c) 19 μs.

Figure 3.14: Volume displacement inside the solid.

Thermal expansion and volume displacement

Total temperature(T_t) obtained is coupled to the solid mechanics:thermal expansion module to solve for solid displacement inside the body. The Fig. 3.13(c) shows a successful coupling between the Navier-Stokes and solid mechanics module at 17.1 μs. Fig. 3.14 display time shots of the total volume displacement achieved inside the solid due to alternating compression and rarefaction originating from the thermal oscillation.

TA signal generation and propagation

The normal component of the stress (time shots shown in Fig 3.15) deduced from the stress strain relation inside the solid undergoing thermal expansion-rarefaction is used to compute the domain source for transient TA signal generation. The nonlinear source-term has the unit of s^{-2}. The time-shots of the source term is demonstrated as Fig 3.16. The TA signal evolves in the solid and propagates through both the solid and liquid media as shown in Fig 3.17.

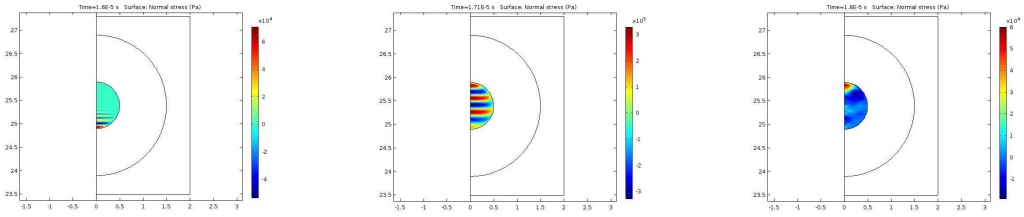

(a) 16 μs. (b) 17.1 μs. (c) 18 μs.

Figure 3.15: Normal component of stress generated from thermal expansion and rarefaction.

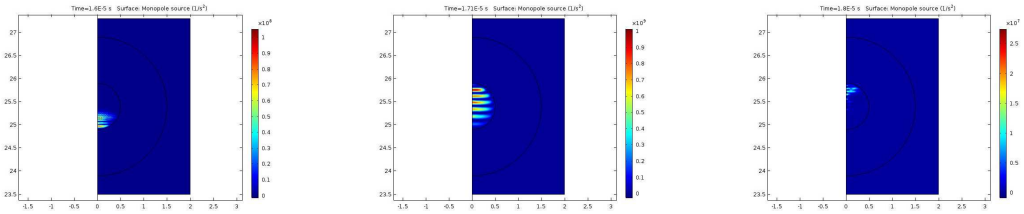

(a) 16 μs. (b) 17.1 μs. (c) 18 μs.

Figure 3.16: Time shots of the evolution of TA domain source.

Quantitative analysis: 1D transient solution data and Fourier analysis.

Fourier domain evaluation of the transmit and receive signal can provide vivid insight. 1D point data are extracted from the solution of different modules. Temporal transmit pressure point data at the center of the solid in question is deduced to evaluate their frequency spectrum. The focal pressure originating from a 100 kPa 2 cycle 5 MHz input pulse (Fig. 3.18(a)) and its Fourier counterpart is depicted in Fig. 3.18(b). Fig. 3.18(c) shows the temporal variation of temperature at the focus as well as the point displacement. The focal pressure measured for a 100 kPa 2 cycle 5 MHz pulse is around 1.2 MPa with a corresponding peak temperature of 120° mK. The thermal expansion results in a maximum total peak displacement of approximately 4 nm. The normal stress derived from the expansion-rarefaction has a peak value of 300 kPa which yields a TA peak pressure of approximately 1.6 kPa. Fig 3.18(e) demonstrates the thermoacoustic signal and its Fourier response. The result establishes the theory, as the Fourier spectrum has a strong DC component and a pass-band close to 2 MHz. In order to verify the square law dependence of the TA signal on the input change, the computations were repeated for peak input pressure of 200 kPa and 400 kPa. Fig. 3.18(f) shows the match of the output data

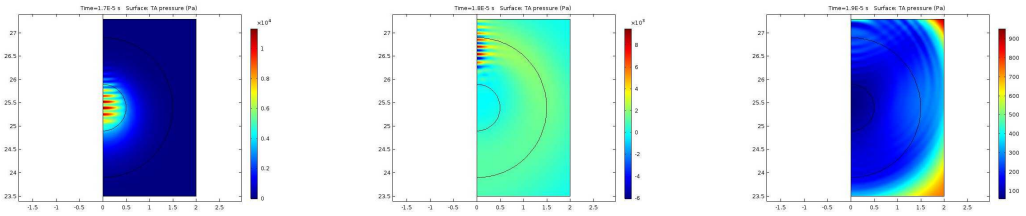

(a) 17 μs. (b) 18 μs. (c) 19 μs.

Figure 3.17: TA signal evolution and propagation.

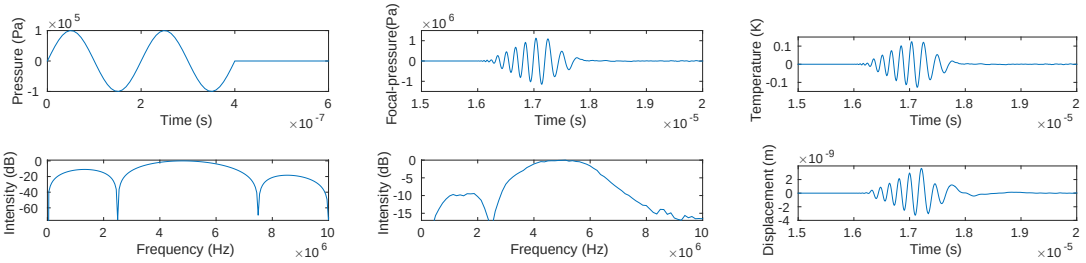

(a) Applied surface pressure: 2 cycle 5 MHz pulse. (b) Focal pressure variation. (c) Focal Temperature and Displacement.

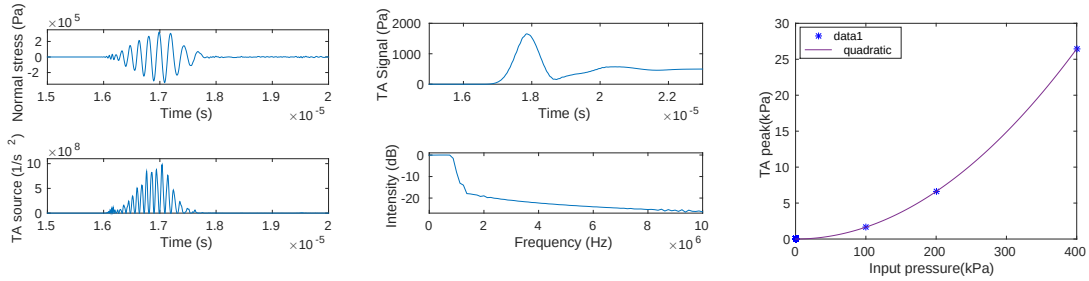

(d) Normal stress and TA source term. (e) TA signal for 100kPa input. (f) Square variation of TA signal.

Figure 3.18: Quantitative analysis of volume generated TA signals from HIFU-TA model.

with the MATLAB quadratic trace.

Directivity of TA signal

Since the measurement is done at orthogonal position w.r.t the source, the scattered components are not present; unlike the simpler point source model shown previously. Even though one does not expect to see the scattered signal at orthogonal position, they are present in the direction of the incident pressure shown in Fig 3.19. The plots demonstrate that the TA signal generated has finite directivity. The pressure envelop is highest along the direction of the incident signal which is an expected result. Fig 3.19(a) shows the point and boundary arcs where Fig 3.19(b) and (c)

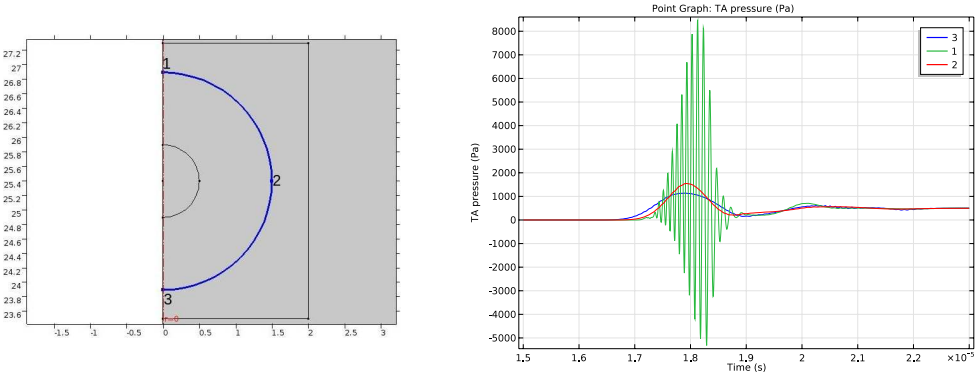

(a) Point locations and arc for measuring and realizing directivity TA measurement.

(b) Point plots showing TA signal spatial variation.

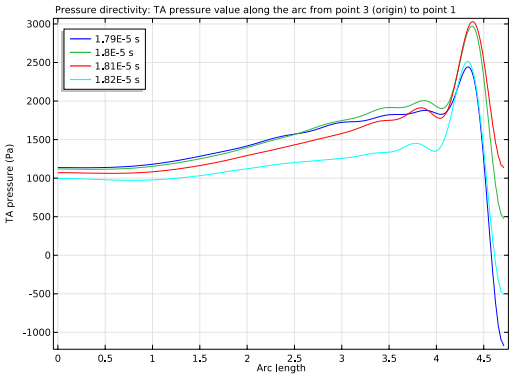

(c) Time wise TA plot shows exhibits directivity of TA pressure.

Figure 3.19: Directivity evaluation of output TA. In (c) arc origin corresponds to point 3 in (a).

has been generated respectively. The origin point in (c) coincides with the point 3 in the figure. It is evident from the figures that the peak pressure is maximum in the incident direction. For the 100 kPa input the peak pressure at the orthogonal position is approximately 1.6 kPa where as at point 3 it is around 1.1 kPa at 1.8 μs.

3.5.3 Metals

Metals can be approximated as thermoelastic materials with very high viscosity. Thus an interesting problem would be to analyze whether metals can produce any TA signal with HIFU excitation. Metals are stiffer in terms of viscosity, thermal expansion and other material properties. But on the contrary the thermal conductivity of metals are considerably higher. To evaluate the TA behavior of metals under pulsed HIFU excitation, the simulations were repeated but with copper as a metal bead in place of silicone glue stick. The material properties are shown below

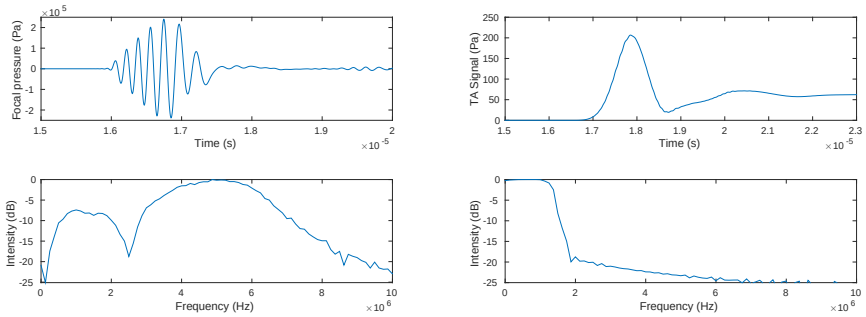

(a) Focal pressure for 100kPa 2 cycle 5MHz input.

(b) TA signal.

Figure 3.20: TA signal generation in Copper for 100 kPa 2 cycle 5 MHz input.

in Table. 3.3. The thermal expansion coefficient of copper is considerably less than

Table 3.3: Property parameter of Copper bead

Parameter	**Value**
Velocity of sound	3560 m/s
Density	8960 Kg/m^3
Specific heat	384 J/Kg-K
Thermal conductivity	401 W/m.K
Coefficient of thermal expansion	16.5×10^{-6}
Bulk viscosity	800 Pa-s
Dynamic viscosity	1200 Pa-s
Young's modulus	120 GPa
Poisson's ratio	0.34
β_1	14

that of silicone glue. Additionally, the thermal conductivity being very high, the cooling procedure in metals is faster. Thus the volume displacement is lesser in magnitude and thus is the peak TA pressure. When the material is changed from copper to other stiffer metals the TA pressure gradually vanishes. However, in case of softer alloys (not pure copper) the TA signal is stronger. In case of glue stick the focal pressure for 100 kPa 2 cycle input was 1.2 MPa and the TA peak value was approximately 1.6 kPa. However for copper, identical input yields 220 kPa focal incident pressure and a TA signal peak amplitude of approximately 230 Pa, even though in both the cases of metal and glue; the waveform and their respective Fourier spectrum are identical. Fig. 3.20 depicts the same.

Chapter 4

Model Verification by Experimental Data

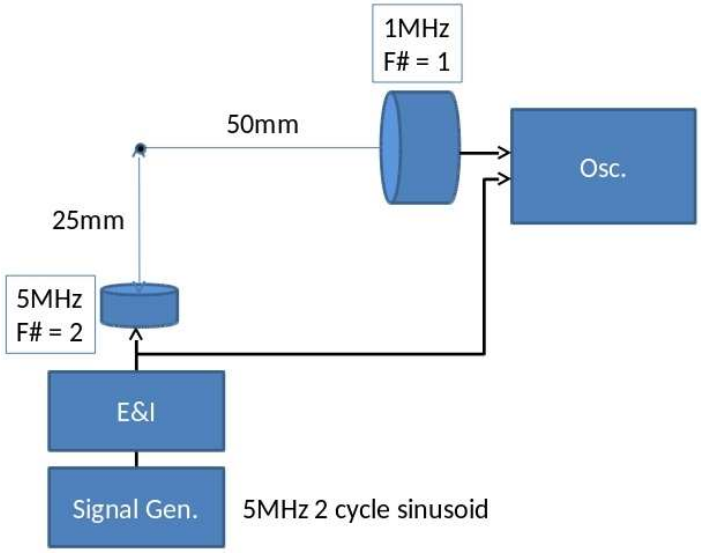

Figure 4.1: A schematic representation of the experimental setup.

The all-acoustic thermoacoustic imaging modality was first porposed by Prof. Mustafa Karaman of Istanbul Technical University (ITU), and first experimental evidence was provided by experiments conducted by himself and Prof. Arif Sanli Ergun at TOBB-ETU, Ankara. A single element F-2 curved piezoelectric transducer with 5 MHz center frequency, 12.5 mm diameter was excited by a 2 cycle 5 MHz sinusoidal pulse. A silicone glue stick was immersed in water at the focus of the transmit transducer. The thermoacoustic signal was detected by a F-1 transducer

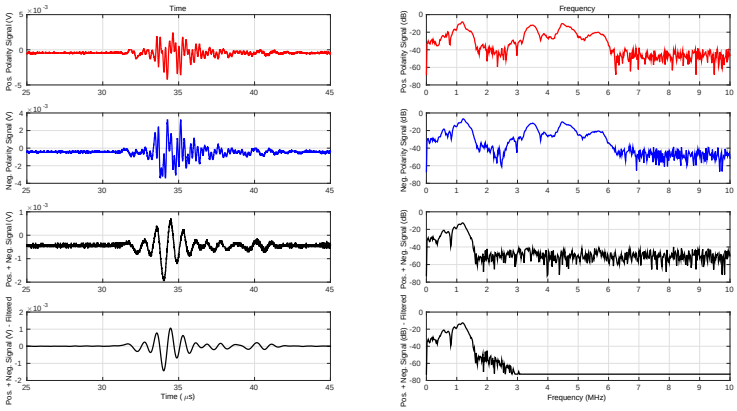

Figure 4.2: TA signals received by a 1 MHz receive transducer for 200 mV 2.5 cycle input drive signal at 5MHz.

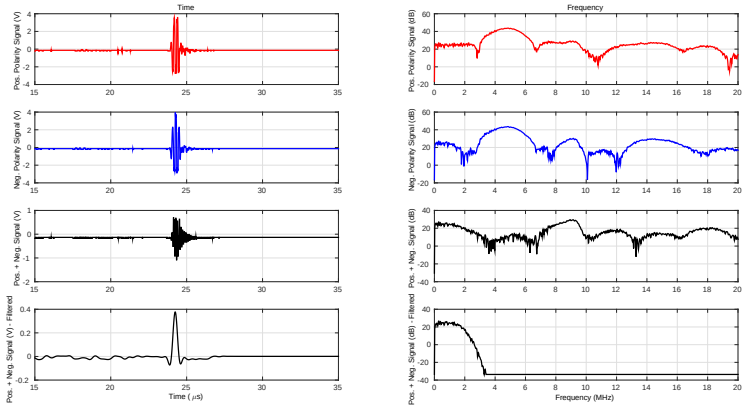

Figure 4.3: TA signals received by hydrophone for 200 mV 2.5 cycle input drive signal at 5MHz.

with a 1 MHz center frequency and 50 mm diameter, which was placed at orthogonal position and the data was collected by an oscilloscope. The schematic representation of the experimental setup is shown in Fig. 4.1. Both the positive and negative polarity signals were fed to the transmit transducer and the TA signals were recorded and the frequency spectra were examined. The separate horizontal set of images(2 in each set) in Fig 4.2 represents:

(red)- Positive polarity excitation induced TA signal and its frequency spectrum;

(blue)- Negative polarity excitation induced TA signal and its frequency spectrum;

(top black)- (Pos - neg) polarity TA signal and its frequency spectrum;

(bottom black)- Filtered (pos + neg) polarity TA and its frequency spectrum.

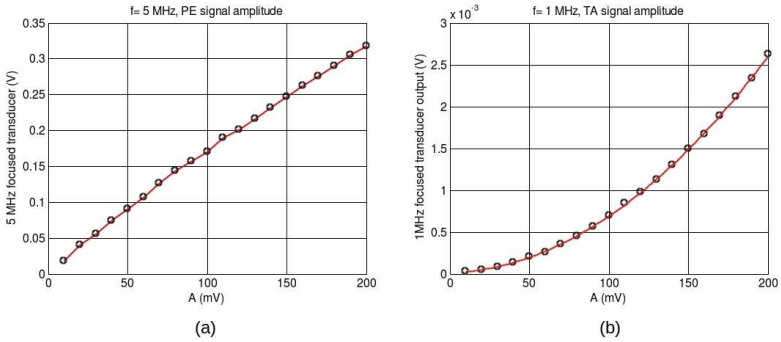

Figure 4.4: Comparison on signal sweep between pulse echo and thermoacoustic signal: (a) Pulse-echo responsehas a linear dependence (b) TA response has a parabolic dependence on the amplitude of the excitation signal.

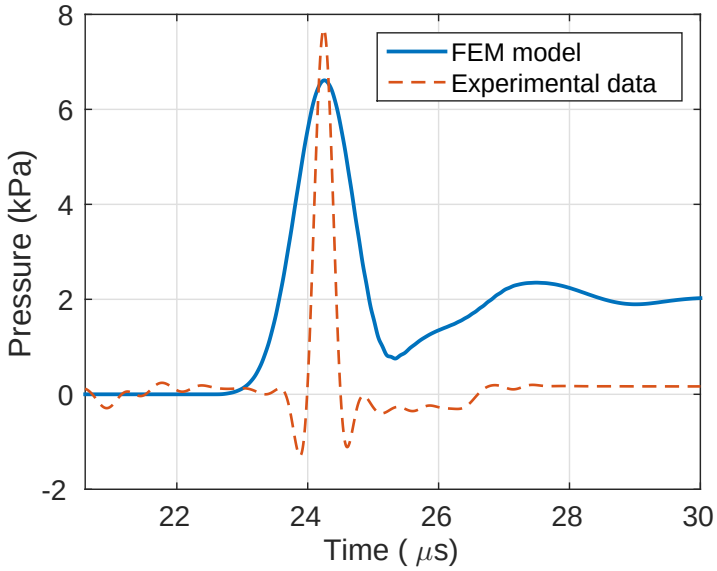

Figure 4.5: Comparison between TA signal from modeling and experiment. Red dashed line shows the experimental data.

The fact that the receive transducer operates at around 1 MHz will certainly force the received signal to be in this frequency band. To guarantee the authenticity of the TA signal measurements the experiments were repeated using a broadband hydrophone. The results are exhibited in Fig 4.3. The labeling are the same as were described for Fig 4.2. Additionally, the voltage sweep response for pulse echo signal and thermoacoustic signal were compared. As proposed by the FEM model the TA output has a parabolic dependence on the input, where as the pulse echo signal varies linearly which is in accordance with the proposed theory. The results are displayed in Fig 4.4. A comparitive plot as shown in Fig 4.5 is also exhibitted. The

blue plot demonstrates the modeling result and the red one shows the experimental data.

Chapter 5

CMUT for HIFU

Piezoelectric transducers (as used in above mentioned experiments and modeling) have certain disadvantages, especially when used for HIFU transmission, which is required proposed AA-TAI modality. Firstly, the acoustic mismatch between the available piezoelectric materials and any loading medium is of concern, for which matching layers are needed. Secondly, integrating a piezoelectric element or transducer to any system is problematic, as established micro-fabrication techniques cannot be used. Additionally backing layers incorporate back-scattering too. In context, recently developed capacitive transducers named Capacitive Micromachined Ultrasonic Transducers (CMUTs) have proven to be advantageous for HIFU [37]. CMUTs have wider bandwidth and effective transmission. Even though therapy generally needs a single operating frequency, broader bandwidth provides probation for dual modality therapy-imaging applications. CMUTs also exhibit less self-heating than piezoelectric transducers. Piezoelectric devices also have high dielectric losses compared to CMUTs.

Capacitive transducers were built initially with conventional machining tools constituting a metal surface as the back electrode and a Mylar membrane forming the top electrode [38]. First generation micro-machined versions of capacitive transducers were introduced and named as CMUTs in 1994 to differentiate them from their piezoelectric counterparts [39] and were manufactured using the sacrificial release process. Even though wafer bonded CMUTs have been reported more recently and gained substantial attraction, sacrificial release process still remains to be a solid micro-fabrication tool for immersion CMUTs. The sacrificial release process

starts with the definition of the vacuum gap of the device by patterning a layer of sacrificial material on the substrate. Later, a con-formal layer of membrane material is deposited, sealing the sacrificial layer. This layer separates the subsequently deposited electrode from the vacuum gap. A second deposition seals the electrodes, after which etch holes are opened for sacrificial release. These etch holes are, then, sealed with a final layer of membrane material deposition, defining the full thickness of the membrane.Both the electrostatic force applied to the CMUT membrane in transmit, and the magnitude of the electrical output of the device in receive modes are a function of the ratio between the applied bias voltage to the instantaneous gap [40]. It is, hence, preferable to reduce the gap between the top and bottom electrodes of the CMUT for reducing voltage levels in transmit mode, and increasing the signal strength in receive mode [41,42]. The distance between the two electrodes are limited by the effective gap height which equals to the summation of the vacuum gap, and the insulating layer thickness scaled by the dielectric constant. Keeping the bias voltage and other device geometry parameters identical, a device with comparatively thinner insulation layer benefits from increased electric field and device capacitance as the effective gap height is reduced [42]. This results in a transducer with relatively higher transmit and receive sensitivity. Improved output sensitivity to decrease the required drive and bias voltage levels, and minimized stray capacitance to reduce the power consumption of the drive electronics are the two main prerequisites of a CMUT arrays based HIFU array. To meet the former objective, the only free transducer parameter is the insulation layer thickness. Results shown in Fig. 5.1 reveal that the collapse voltage under atmospheric pressure decreases from 124 V to 87 V as the first insulation film thickness is reduced from 600 nm to 200 nm. The thinning of the insulation film provides a substantial improvement in output sensitivity. Values shown in the plot are calculated by setting the DC bias to 80% of the collapse voltage. Based on the results shown in Fig. 5.1, we conclude that the bias voltage requirement and output sensitivity of the particular CMUT device can be improved by thinning the insulation layer without compromising the electrical safety of the dielectric material.

The sacrificial release method has an inherent shortcoming in reducing insulation layer thickness, as the film needed for sealing the sacrificial layer from the device

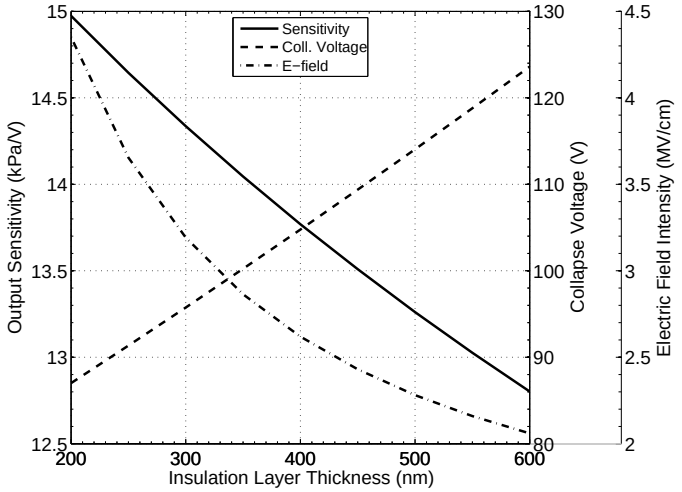

Figure 5.1: Dependence of collapse voltage, electric field intensity and output sensitivity to the insulation layer thickness.

electrode needs to be comparatively thicker than the sacrificial structures due to conformality issues. This results in a mechanically weak membrane at the perimeter, incapable of protecting the electrode material from the potential corrosive effects of the etchant used during release. The under-etch step cannot precede the electrode and subsequent membrane deposition steps, as it will result in a structurally weak thin dielectric layer which cannot withstand the processes involved in membrane release. To alleviate this problem, methods for modifying CVD recipes for better con-formality have been reported [43]. Compensation of the effect of a thick insulation layer by the use of high dielectric constant materials such as Hafnium(IV) oxide (HfO_2) have also been suggested [42], but these still require a con-formal film.

In due context, a micromachining method is proposed which mitigates the conformality requirement on the CVD films for the fabrication of CMUTs by burying metallic films into structural layers. The method facilitates flat surfaces for subsequent processing which enables the construction of (1) thinner insulating films to increased device sensitivity, and (2) patterned back electrodes for reducing stray capacitance. The technique also alleviates issues resulting from bent structures [44].

5.1 Fabrication Issues

Initial manufacturing efforts were conducted using the conventional sacrificial etch technique. Process steps are depicted in Fig. 5.2. The chromium sacrificial layer is

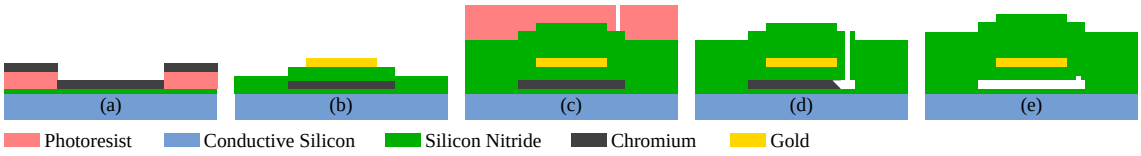

Figure 5.2: Process steps for conventional CMUT fabrication: (a) Bottom insulator deposition followed by sacrificial patterning, growth and lift-off, (b) insulation layer growth and electrode patterning, (c) etch hole lithography, (d) sacrificial underetch, (e) final membrane deposition and sealing.

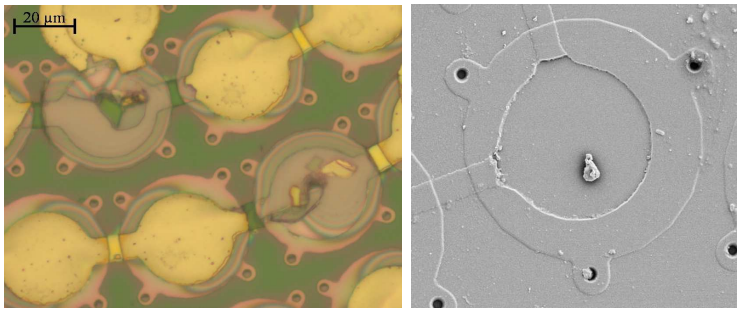

Figure 5.3: Harm caused by the chromium etchant on the Cr-Au electrode. The micro-graph on the left shows that the Cr adhesion layer beneath the Au top electrode has been removed by the etchant so that the top electrode breaks apart when wiped with a cotton swab. The SEM image on the right was taken from a similarly damaged sample. The insulation layer on the vacuum gap is still intact. The interconnect line is seen to have a hollow opening through which the etchant has apparently flown.

patterned on an initial Si_3N_4 insulation layer coating a p-type low resistivity (0.01-0.02 Ω-cm) silicon wafer. This is followed by the deposition of the first structural Si_3N_4 layer, which also acts as an insulator. This step is followed by electrode patterning which are then buried under another Si_3N_4 film. The process is completed by the opening of the etch holes, the sacrificial release, and a final sealing deposition. To minimize the adverse effects of the insulation layer on device sensitivity, patterned chromium sacrificial islands of 200 nm thickness were coated with a 300 nm thick Si_3N_4 film. After underetch, substantial peeling was observed at the edges of the top electrodes of the device, even though they were buried under a Si_3N_4 film of 600 nm thickness, as shown in Fig. 5.3. This discrepancy was attributed to the conformality of the deposited Si_3N_4 film. The manufacturing process which require the patterning of films of films of varied thickness (few 100 nm - few μm) at various steps, results in height variations on the wafer surface. The coating on the sacrificial islands which forms the insulation layer consequently after release has to be tightly encapsulating to protect the top electrode from the harm of the sacrificial etchant. Even though

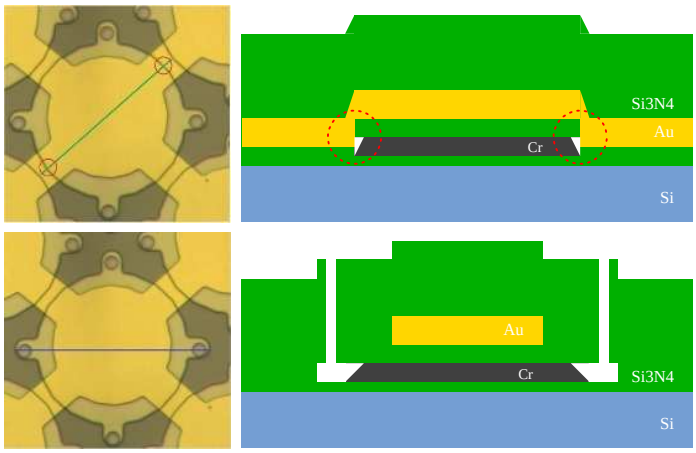

Figure 5.4: A non-conformal film results in the top electrode getting into contact with the sacrificial layer, and consequently being harmed by the etchant.

PECVD dielectric thin films are claimed to be conformal for any thickness being deposited, there has been reported cases as evidence of the side walls being thinner than the horizontal layer on the structures, especially when the structures below are a few hundred nanometers thick, and hence creating void [45]. The problem associated with the film thickness is the electrode getting into contact with the sacrificial layer from the sidewall region of the sacrificial islands, which gives a substantial harm to the electrode during underetch, as shown in Fig. 5.4. The same harm would have been observed when KOH is used as the sacrificial etchant, as KOH is known to harm Cr and Ti. [46, 47]. The conventional devices fabricated on conducting wafers also had high levels of parasitic capacitance due to interconnect lines and connection pads outside the active device area, due to which an array element with 5 pF active device capacitance results in an electrical load as high has 28 pF. A workaround for this issue is the use of totally insulating or SOI wafers onto which a back electrode layer would be grown. As the back and top electrodes would only overlap over the active device area, stray capacitance would be significantly reduced. Consequently, a method for the manufacturing of buried back electrodes is developed. The membrane material was chosen as PECVD Silicon Nitride (Si_3N_4), grown using an Oxford PlasmaLab System 100 deposition system. Table 5.1 lists the deposition parameters. The dual frequency pulsed deposition recipe yields a low stress membrane. A KLA-TENCOR P6 Surface Profiler was used the asses the post deposition stress build-up in multi-layer films. An average value of 132 MPa of tensile stress was measured, which is consistent with values reported in the literature [48,

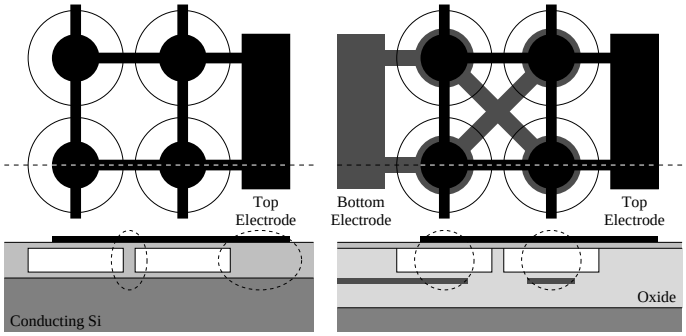

Figure 5.5: CMUTs on conducting substrates inherently suffer from stay capacitance created by interconnects and pads outside active device area (left.) The problem can be alleviated by the growth of a non-overlapping explicit back electrode in an insulating layer (right.)

Table 5.1: PECVD Silicon Nitride Deposition Parameters

Parameter	Value
SiH_4/N_2 (5%/95%) Flow Rate	400 sccm
NH_3 Flow Rate	20 sccm
N_2 Flow Rate	600 sccm
Chamber Pressure	650 mTorr
HF (13.56 MHz) Duration	14 seconds @ 20 W
LF (380 kHz) Duration	6 seconds @ 20 W
Table Temperature	300°C
Deposition Rate	10 nm/min

49]. The PECVD deposition system provides excellent control on the growth rate, and, hence, the film thickness. The mass density of the Si_3N_4 film was calculated as 2280 kg/m^3 based on the pre- and post-deposition weight of the wafer, which was measured using a Sartorius CPA224S scale with 0.1 mg resolution. Using test structures comprising sandwiched dielectric layers between electrodes, the dielectric constant of the film was measured as 6.2. The sacrificial material opted for our process is chromium due to low process temperature requirements, and increased selectivity. A commercially available etchant (TechniStrip Cr01 by Microchemicals GmbH, Ulmis used for the removal of the chromium sacrificial layer. PECVD Si_3N_4 films and silicon substrates are fully inert to the etchant. Electrodes are made of gold, with chromium used as the adhesion layer. A TORR E-beam and Thermal Evaporator has been used for the growth of metallic films. Etch holes for sacrificial release are opened using an Oxford Plasma Lab 100 ICP 300 RIE/ICP system. The recipe is shown in Table 5.2.

Table 5.2: Silicon nitride etching parameters

Parameter	Value
SF_6 Flow Rate	45 sccm
Chamber Pressure	7.5×10^{-9} Torr
DC Power	50 W
RF Power	2000 W
Table Temperature	10°C
Etch Rate	8 - 10 nm/sec

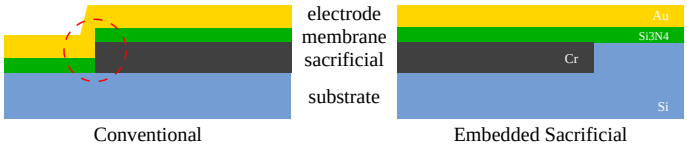

Figure 5.6: The conventional fabrication method requires a first silicon nitride layer to be at least as thick as the sacrificial to separate the device electrode from the sacrificial layer. A nonconformal thinner layer produces a profile as marked by the dashed circle. The proposed method alleviates this problem by embedding the sacrificial layer.

5.1.1 CMUTs with Embedded Sacrificial Layers

As a solution to the problem associated with the conventional process, a micromachining technique is proposed where the metallic sacrificial layer is embedded into the substrate to provide a topology free surface, obviating the conformality requirement (Fig. 5.6). The results of this technique were published in [50]. The process steps of the moderated fabrication procedure are depicted in Fig. 5.7. We start with the deposition of 300 nm of insulating Si_3N_4 layer which can act both as the etch stop layer during release and as an insulator during device operation. This is followed by an image reversal lithography with the sacrificial pattern mask on the insulator coated silicon wafer succeeded by a 100 W descum for 20 seconds. The next step is a controlled RIE process which opens up approximately 200 nm deep grooves in the shape of the sacrificial patterns. Finally, 200 nm of chromium is evaporated, which is followed by lift-off. Hence, the etching of the grooves and the deposition of the sacrificial layers are done with a single lithography step making the grooves and the sacrificial layer self-aligned. Sacrificial embedding is followed by the deposition of the first structural Si_3N_4 layer, whose thickness is set to 200 nm. We, then, patterned the Cr/Au top electrode of 20 nm/150 nm thickness. The electrodes are then buried under another 600 nm thick Si_3N_4 film. We have used a positive lithography

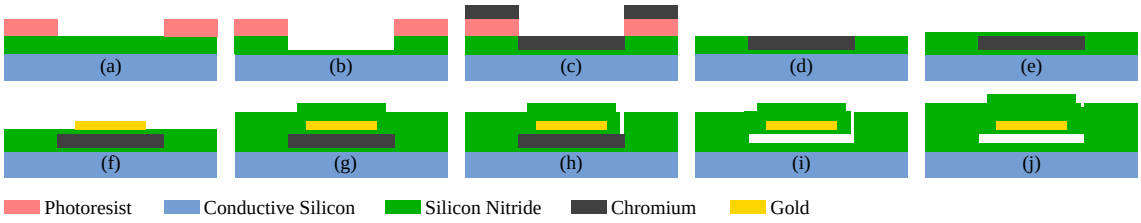

Figure 5.7: Process steps for embedded sacrificial technique: (a) Image reversal lithography with sacrificial mask on insulating nitride; (b) DRIE defines 200 nm deep sacrificial grooves; (c) 200 nm Chromium evaporation; (d) Liftoff and cleaning; (e) First nitride layer deposition; (f) Top electrode deposition and patterning; (g) Burying electrode under thick nitride; (h) Etch via patterning and etching; (i) Underetching, release and drying; (j) Final sealing layer deposition. The top layer covering aids also in reaching the needed membrane thickness.

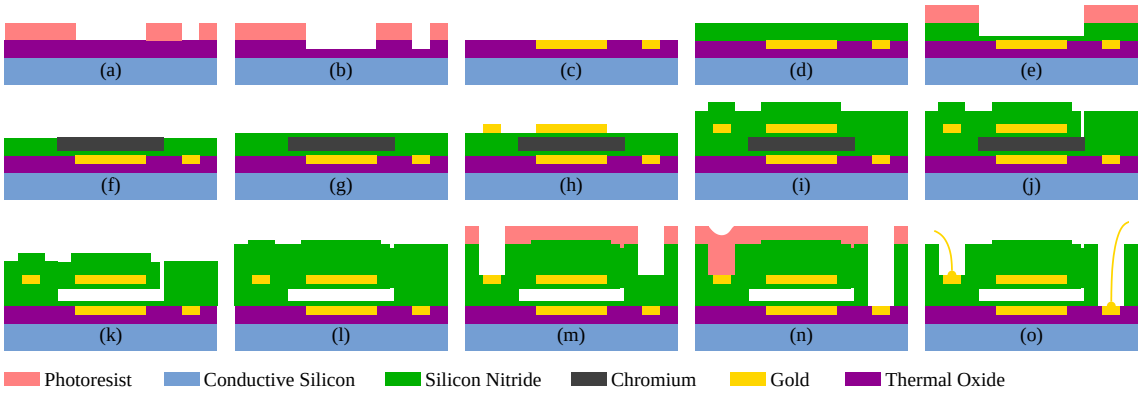

Figure 5.8: Process steps for devices made by embedded sacrificial technique made with separate bottom electrodes. (a) Lithography on a thermally oxidized Si wafer, (b) RIE for groves, (c) Au/Cr deposition and lift-off. Steps (d)-(m) follow the procedure in Fig. 5.7. An additional lithography and RIE is required to expose and wire bond the back electrode, as in (n) and (o).

step to pattern the etch holes which are opened up by an RIE step. Afterwards, the sample is set for underetching and release. The etchant is flushed using methanol to avoid stiction. After proper drying, the devices are coated with another thick layer of silicon nitride to seal the holes and to reach the required membrane thickness.

5.1.2 CMUTs with Embedded Back Electrodes

To reduce spurious capacitance, devices were fabricated on thermally oxidized silicon wafers as suggested in [41], but by burying the metallic back electrode of the device into the oxide layer by the embedding technique. For these devices, the top and bottom electrodes overlap only at the active device area, which substantially reduces the parasitic capacitance (Fig. 5.5). Embedding the back electrode enables the

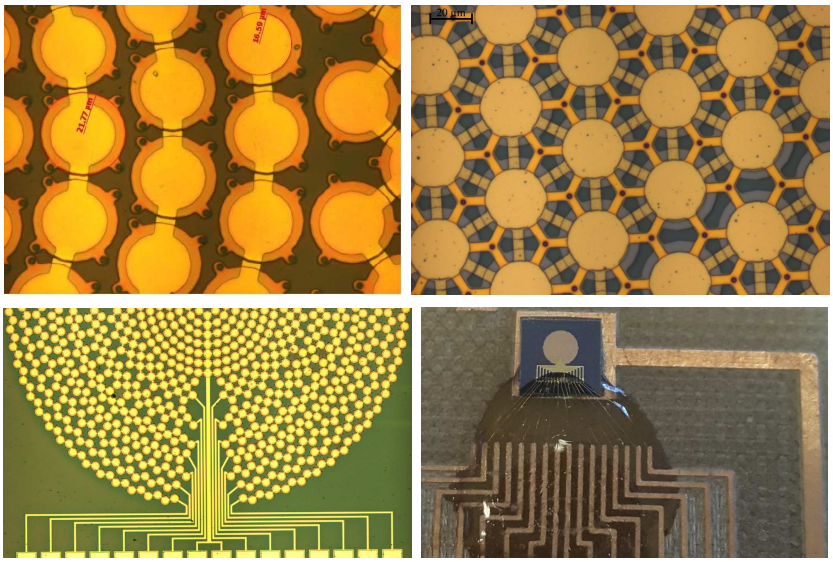

Figure 5.9: Optical micrographs of sealed devices on conductive substrate (top left) and thermally oxidized wafer (top right). CMUT ring array (bottom left), wire bonded and insulated device (bottom right).

growth of a thin insulation layer on the electrode, and provides a flat surface for subsequent steps, which are identical to those used in the manufacturing of devices on a conducting substrate. The steps of the process are depicted in Fig. 5.8.

5.2 Results

Optical micrographs of sealed devices without and with embedded back electrodes, and wire bonded devices ready for testing are shown in Fig. 5.9. Few of the sample devices (with and without separate bottom electrodes) manufactured using the embedded sacrificial technique were finely broken to facilitate a cross-section view. Fig. 5.10 shows the SEM pictures of these devices. The measured thicknesses of the vacuum gap and the initial nitride layer are both 212 nm for the first sample, while the insulating layer is thinner than the gap in the other two samples.

5.2.1 Improvement in Output Sensitivity

As a verification for device sensitivity, a transducer with membrane and insulation layer thicknesses of 1.7μm and 350 nm, respectively, and collapse voltage of approximately 100 V was immersed in sunflower oil and each element of the array were driven with 20 V_{pp} signals at 7.5 MHz while the DC bias was set to 80 V. Individual

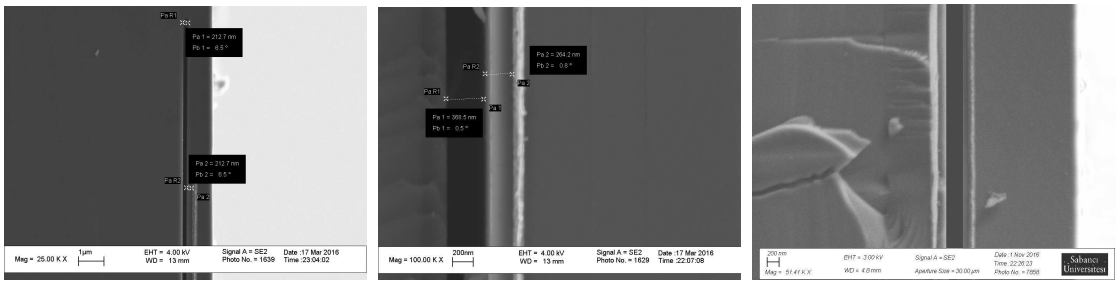

(a) CMUTs with equal gap and insulation.

(b) CMUT with thinner insulation..

(c) CMUT with thinner insulation and back electrode.

Figure 5.10: SEM of manufactured CMUT device. The gap and silicon nitride layer beneath the electrode is visible. Measurements indicate that the initial nitride film is as thick as the vacuum gap which is only possible by the embedded sacrificial layer method (top.) The image at the center shows the cross section of a test device where a comparatively thinner insulation layer was achieved. The third figure is an SEM cross section of a device with separately embedded bottom electrode; which also exhibits a thinner insulation in comparison to the vacuum gap height.

drive signals were phased to focus the transducer to 1.5, 2.0, and 3.5 mm, respectively. For each setting, the focal pressure was measured as 1300, 990, and 830 kPa, using an Onda HNP-0200 hydrophoneThe focusing gain from the transducer surface to the hydrophone tip of 200 μm diameter was calculated as 5.91, 4.94, and 2.86 for the respective focal distances, using the plane wave decomposition method. The attenuation in sunflower oil was taken as 1.38×10^{-7} NPs/cm [51]. Consequently, the measured focal pressure values correspond to 220, 200, and 290 kPa of pressure measured at the transducer surface, respectively. Based on the analysis result of Fig. 5.1, the DC bias requirement of the manufactured device is about 19% smaller than that of a transducer with an insulation layer of 600 nm thickness, while the output sensitivity is higher by 10%. The device can generate 14 kPa/V of pressure, which is comparable to the efficiency of commercially available piezoelectric transducers, but does not require a matching layer, and, hence, is smaller in physical dimensions. Combined with significantly decreased self heating, the CMUT is a viable alternative for HIFU applications.

5.2.2 Reduction in Parasitic Capacitance

Device capacitance for both type of arrays (with and without separate bottom electrodes) were measured separately with an Agilent 4294A Impedance Analyzer.

Measurements were performed on unbiased transducers. For the devices fabricated on conducting silicon wafer the capacitance of one array element (comprising 170 CMUT cells) is 28 pF, while for the device array manufactured with separately embedded gold bottom electrodes the capacitance is measured as 11 pF. Consequently, stray capacitance is reduced from 22 pF to 6 pF, which is in excess of 70%.

Chapter 6

Conclusion

This dissertation establishes the theoretical and numerical basis for a novel thermoacoustic imaging modality which uses ultrasound as the heat source. A forward transient theory is developed and a full set of governing equations are proposed for:

1. Ultrasonic pulse propagation and target heating leading to temporal thermal oscillations;
2. Thermal expansion of target, volume displacement;
3. TA signal generation, propagation and evaluation.

The coupled Navier-Stokes equation are solved under the light of linear perturbation theory using COMSOL Multiphysics®(a commercially available FEM package) to evaluate the thermal oscillation at the target. The results obtained are used to solve the thermal expansion and rarefaction of the solid medium immersed in fluid. Finally the TA signal generation and propagation are solved using the nonlinear wave equation. At first a simple point source model is used to prove the feasibility of the proposed modality. Later, in a separate model pulsed HIFU heating is used as the excitation mean. Some simple experimental results are used to validate the model. To the best knowledge of the author, a forward transient working model exhibiting the feasibility of ultrasound driven thermoacoustic imaging procedure gas not been proposed or demonstrated in available literature. The target material is chosen to be silicon glue stick immersed in water. Simulation results are in close agreement with experimental data. It is seen that the thermoacoustic signal scales with parabolic dependance on the input signal as the TA signal approximately follows the envelop of the normal stress component (or pressure) originating from the thermal expansion

gradient. This insight is also available in the spectral analysis results of the output signal. Additionally, metals were also tried as target objects and in due agreement with experimental verification it was infered that softer metals with high viscosity can also absorb sound pulses and generate TA signals. If the current modality has to be established as a feasible option for biomedical imaging and NDE, a proper image reconstruction algorithm has to be developed, which remains a open problem. Once developed, the present work can be expanded to a HIFU-TA based imaging device design and prototyping. However rigorous experimentation and analysis are needed before something similar can be established. As HIFU is the incident energy, high efficiency capacitive micromachined ultrasonic transducers(CMUTs) with high transmit sensitivity are fabricated with important development on established micromachining techniques and hence solving a standing problem. These ring array transducers have demonstrated strong HIFU capabilities and can be used in the AA-TAI device prototype for both transmit and receive. In conclusion, this novel technique of all ultrasound thermoacoustic imaging has immense research and development potential.

Bibliography

[1] Mark W. Zemansky, *Heat and Thermodynamics*, McGraw-Hill Book Company, 1957.

[2] T. Bowen, "Radiation-induced thermoacoustic soft tissue imaging," in *1981 Ultrasonics Symposium*, Oct 1981, pp. 817–822.

[3] Lord J.W.S Rayleigh, *The Theory of Sound; Vol:2*, London: Macmillan, 1894.

[4] C. Sondhauss, "Ueber die schallschwingungen der luft in erhitzen glasrohren und in gedeckten pfeifen von ungleicher weite," *Annalen der Physik*, vol. 155, no. 1, pp. 1–34, 1850.

[5] Alexander Graham Bell, "On the production and reproduction of sound by light," *American Journal of Physics*, vol. 20, no. 118, pp. 305–324, Oct 1880.

[6] T. Bowen, R. L. Nasoni, and A. E. Pifer, *Thermoacoustic Imaging Induced by Deeply Penetrating Radiation*, pp. 409–427, Springer US, Boston, MA, 1984.

[7] X. Wang, D. R. Bauer, R. Witte, and H. Xin, "Microwave-induced thermoacoustic imaging model for potential breast cancer detection," *IEEE Transactions on Biomedical Engineering*, vol. 59, no. 10, pp. 2782–2791, Oct 2012.

[8] Richard G. Olsen and James C. Lin, "Acoustical imaging of a model of a human hand using pulsed microwave irradiation," *Bioelectromagnetics*, vol. 4, no. 4, pp. 397–400, 1983.

[9] Da Xing and Liangzhong Xiang, "Photoacoustic and thermoacoustic imaging for biomedical applications," in *2007 Asia Optical Fiber Communication and Optoelectronics Conference*, Oct 2007, pp. 227–229.

[10] Z. Wang, S. Ha, and K. Kim, "Evaluation of finite element based simulation model of photoacoustics in biological tissues," in *SPIE Proceedings 8320: Medical imaging*, Feb 2012, pp. 1L–9L.

[11] Lei Yao and Huabei Jiang, "Finite-element-based photoacoustic tomography in time domain," *Journal of Optics A: Pure and Applied Optics*, vol. 11, no. 8, pp. 085301, 2009.

[12] Robert A. Kruger, Pingyu Liu, Yuncai Richard Fang, and C. Robert Appledorn, "Photoacoustic ultrasound (paus)reconstruction tomography," *Medical Physics*, vol. 22, no. 10, pp. 1605–1609, 1995.

[13] Robert A. Kruger, Daniel R. Reinecke, and Gabe A. Kruger, "Thermoacoustic computed tomographytechnical considerations," *Medical Physics*, vol. 26, no. 9, pp. 1832–1837, 1999.

[14] Robert A. Kruger, Kenyon K. Kopecky, Alex M. Aisen, Daniel R. Reinecke, Gabe A. Kruger, and Jr William L. Kiser, "Thermoacoustic ct with radio waves: A medical imaging paradigm," *Radiology*, vol. 211, no. 1, pp. 275–278, 1999, PMID: 10189483.

[15] Robert A. Kruger, Kathy D. Miller, Handel E. Reynolds, Jr William L. Kiser, Daniel R. Reinecke, and Gabe A. Kruger, "Breast cancer in vivo: Contrast enhancement with thermoacoustic ct at 434 mhzfeasibility study," *Radiology*, vol. 216, no. 1, pp. 279–283, 2000, PMID: 10887262.

[16] Robert A. Kruger, William L. Kiser, Daniel R. Reinecke, and Gabe A. Kruger, "Thermoacoustic computed tomography using a conventional linear transducer array," *Medical Physics*, vol. 30, no. 5, pp. 856–860, 2003.

[17] Zhong Ji, Cunguang Lou, Sihua Yang, and Da Xing, "Three-dimensional thermoacoustic imaging for early breast cancer detection," *Medical Physics*, vol. 39, no. 11, pp. 6738–6744, 2012.

[18] Xing Jin, Yuan Xu, Lihong V. Wang, Yuncai R. Fang, Claudio I. Zanelli, and Samuel M. Howard, "Imaging of high-intensity focused ultrasound-induced

lesions in soft biological tissue using thermoacoustic tomography," *Medical Physics*, vol. 32, no. 1, pp. 5–11, 2005.

[19] M. Idemen and A. Alkumru, "On an inverse source problem connected with photo-acoustic and thermo-acoustic tomographies," *Wave Motion*, vol. 49, no. 6, pp. 595 – 604, 2012.

[20] Minghua Xu and Lihong V. Wang, "Universal back-projection algorithm for photoacoustic computed tomography," *Phys. Rev. E*, vol. 71, pp. 016706, Jan 2005.

[21] A. Tominaga, "Thermodynamic aspects of thermoacoustic theory," *Cryogenics*, vol. 35, no. 7, pp. 427 – 440, 1995.

[22] Clarence Zener, "Internal friction in solids," *Proceedings of the Physical Society*, vol. 52, no. 1, pp. 152, 1940.

[23] Clarence Zener, "Internal friction in solids ii. general theory of thermoelastic internal friction," *Phys. Rev.*, vol. 53, pp. 90–99, Jan 1938.

[24] J. B. Alblas, "On the general theory of thermo-elastic friction," *Applied Scientific Research*, vol. 10, no. 1, pp. 349–362, 1961.

[25] J. B. Alblas, "A note on the theory of thermoelastic damping," *Journal of Thermal Stresses*, vol. 4, no. 3-4, pp. 333–355, 1981.

[26] V. N. Alekseev and S. A. Rybak, "Equations of state for viscoelastic biological media," *Acoustical Physics*, vol. 48, no. 5, pp. 511–517, 2002.

[27] John D.. Ferry, *Viscoelastic Properties of Polymers*, John Wiley and Sons, 1980.

[28] Robert Zwanzig and Raymond D. Mountain, "Highfrequency elastic moduli of simple fluids," *The Journal of Chemical Physics*, vol. 43, no. 12, pp. 511–517, 1965.

[29] J.C. Simo, "On a fully three-dimensional finite-strain viscoelastic damage model: Formulation and computational aspects," *Computer Methods in Applied Mechanics and Engineering*, vol. 60, no. 2, pp. 153 – 173, 1987.

[30] Pedro Areias and Karel Matou, "Finite element formulation for modeling nonlinear viscoelastic elastomers," *Computer Methods in Applied Mechanics and Engineering*, vol. 197, no. 5152, pp. 4702 – 4717, 2008.

[31] Qinwu Xu and Jorge A. Prozzi, "A time-domain finite element method for dynamic viscoelastic solution of layered-half-space responses under loading pulses," *Computers and Structures*, vol. 160, pp. 20 – 39, 2015.

[32] Anna Perelomova and Weronika Pelc-Garska, "Efficiency of acoustic heating produced in the thermoviscous flow of a fluid with relaxation," *Central European Journal of Physics*, vol. 8, no. 6, pp. 855–863, 2010.

[33] Anna Perelomova, "Acoustic radiation force and streaming caused by non-periodic acoustic source," *Acta Acustica united with Acustica*, vol. 89, no. 5, pp. 754–763, 2003.

[34] Anna Perelomova, "Development of linear projecting in studies of non-linear flow. acoustic heating induced by non-periodic sound," *Physics Letters A*, vol. 357, no. 1, pp. 42 – 47, 2006.

[35] Anna Perelomova, "Acoustic heating in a weakly dispersive fluid flow," *Acta Acustica united with Acustica*, vol. 94, no. 3, pp. 382–387, 2008.

[36] D.T. Blackstock, *Fundamentals of Physical Acoustics*, John Wiley and Sons, 2000.

[37] S. H. Wong, M. Kupnik, R. D. Watkins, K. Butts-Pauly, and B. T. Khuri-Yakub, "Capacitive micromachined ultrasonic transducers for therapeutic ultrasound applications," *IEEE Transactions on Biomedical Engineering*, vol. 57, no. 1, pp. 114–123, Jan 2010.

[38] M. Rafiq and C. Wykes, "The performance of capacitive ultrasonic transducers using v-grooved backplates," *Meas. Sci. Technol.*, vol. 2, pp. 168–174, 1991.

[39] M. I. Haller and B. T. Khuri-Yakub, "A surface micromachined electrostatic ultrasonic air transducer," *IEEE Trans. on Ultrasonics, Ferroelectrics and Frequency Control*, vol. 43, no. 1, pp. 1–6, Jan 1996.

[40] S. Satir, J. Zahorian, and F. L. Degertekin, "A large-signal model for cmut arrays with arbitrary membrane geometry operating in non-collapsed mode," *IEEE Transactions on Ultrasonics, Ferroelectrics, and Frequency Control*, vol. 60, no. 11, pp. 2426–2439, November 2013.

[41] J. Knight, J. McLean, and F. L. Degertekin, "Low temperature fabrication of immersion capacitive micromachined ultrasonic transducers on silicon and dielectric substrates," *IEEE Transactions on Ultrasonics, Ferroelectrics, and Frequency Control*, vol. 51, no. 10, pp. 1324–1333, Oct 2004.

[42] T. Xu, C. Tekes, and F. L. Degertekin, "Cmuts with high-k atomic layer deposition dielectric material insulation layer," *IEEE Transactions on Ultrasonics, Ferroelectrics, and Frequency Control*, vol. 61, no. 12, pp. 2121–2131, Dec 2014.

[43] Min Park, Hyun Kyu Yu, Jin Gun Koo, Jin Jang, and Kee Soo Nam, "High-quality conformal silicon oxide films prepared by multi-step sputtering pecvd and chemical mechanical polishing," *Journal of Electronic Materials*, vol. 27, no. 11, pp. 1262–1267, 1998.

[44] T. Lisec, M. Kreutzer, and B. Wagner, "Surface micromachined piezoresistive pressure sensors with step-type bent and flat membrane structures," *IEEE Transactions on Electron Devices*, vol. 43, no. 9, pp. 1547–1552, Sep 1996.

[45] I. Ali and S. Raghavan, *Integration of CMP into deep submicron multilevel metalization circuits*, vol. 96-22, Proceedings of the First International Symposium on Chemical Mechanical Planarization, The Electrochemical Society Inc., 1997.

[46] K. R. Williams, K. Gupta, and M. Wasilik, "Etch rates for micromachining processing-part ii," *Journal of Microelectromechanical Systems*, vol. 12, no. 6, pp. 761–778, Dec 2003.

[47] P. Walker and W. H. Tarn, *CRC Hand book of metal etchants*, CRC Press LLC, 1991.

[48] E. Cianci, A. Schina, A. Minotti, S. Quaresima, and V. Foglietti, "Dual frequency PECVD silicon nitride for fabrication of CMUTs membranes," *Sensors and Actuators A: Physical*, vol. 127, no. 1, pp. 80 – 87, 2006.

[49] E. Cianci, A. Coppa, and V. Foglietti, "Youngs modulus and residual stress of {DF} {PECVD} silicon nitride for {MEMS} free-standing membranes," *Microelectronic Engineering*, vol. 84, no. 58, pp. 1296 – 1299, 2007, Proceedings of the 32nd International Conference on Micro- and Nano-Engineering.

[50] R. Bardhan Roy, O. Farhanieh, A. S. Ergn, and A. Bozkurt, "Fabrication of high-efficiency cmuts with reduced parasitics using embedded metallic layers," *IEEE Sensors Journal*, vol. 17, no. 13, pp. 4013–4020, July 2017.

[51] Ratjika Chanamai and D Julian McClements, "Ultrasonic attenuation of edible oils," *Journal of the American Oil Chemists' Society*, vol. 75, no. 10, pp. 1447–1448, 1998.